Beyond the relativistic mean-field approximation: Configuration mixing of angular-momentum-projected wave functions

Nikšić, Tamara; Vretenar, Dario; Ring, Peter

Beyond the relativistic mean-field approximation: Configuration mixing of angular-momentum-projected wave functions

T. Nikšić and D. Vretenar
Physics Department, Faculty of Science, University of Zagreb, Croatia, and Physik-Department der Technischen Universität München, D-85748 Garching, Germany

P. Ring
Physik-Department der Technischen Universität München, D-85748 Garching, Germany
(Received 9 December 2005; published 14 March 2006)

We report the first study of restoration of rotational symmetry and fluctuations of the quadrupole deformation in the framework of relativistic mean-field models. A model is developed that uses the generator coordinate method to perform configuration mixing calculations of angular-momentum-projected wave functions, calculated in a relativistic point-coupling model. The geometry is restricted to axially symmetric shapes, and the intrinsic wave functions are generated from the solutions of the constrained relativistic mean-field + BCS equations in an axially deformed oscillator basis. A number of illustrative calculations are performed for the nuclei ^{194}Hg and ^{32}Mg, in comparison with results obtained in nonrelativistic models based on Skyrme and Gogny effective interactions.

DOI: 10.1103/PhysRevC.73.034308 PACS number(s): 21.60.Jz, 21.10.Pc, 21.10.Re, 21.30.Fe

I. INTRODUCTION

The rich variety of nuclear shapes far from stability has been the subject of extensive experimental and theoretical studies. The variation of ground-state shapes in an isotopic chain, for instance, is governed by the evolution of shell structure. Far from the β-stability line, in particular, the energy spacings between single-particle levels change considerably with the number of neutrons and/or protons. This can result in reduced spherical shell gaps and modifications of shell structure, and in some cases spherical magic numbers may disappear. For example, in neutron-rich nuclei $N = 6, 16, 34, \ldots$ can become magic numbers, whereas $N = 8, 20, 28, \ldots$ disappear. The reduction of a spherical shell closure is associated with the occurrence of deformed ground states and, in a number of cases, with the phenomenon of shape coexistence.

Both the global shell-model approach and self-consistent mean-field models have been employed in the description of shell evolution far from stability. The basic advantages of the shell model are its ability to describe simultaneously all spectroscopic properties of low-lying states for a large domain of nuclei, its use of effective interactions that can be related to two- and three-nucleon bare forces, and its description of collective properties in the laboratory frame. However, since effective interactions strongly depend on the choice of active shells and truncation schemes, there is no universal shell-model interaction that can be used for all nuclei. Moreover, because numerous two-body matrix elements have to be adjusted to data, extrapolations to exotic systems far from stability cannot be very reliable. Heavy exotic nuclei with very large valence spaces require calculations with matrix dimensions that are far beyond the limits of current shell-model variants.

Properties of heavy nuclei with a large number of active valence nucleons are best described in the framework of self-consistent mean-field models. A variety of structure phenomena, not only in medium-heavy and heavy stable nuclei but also in regions of exotic nuclei far from the line of β stability and close to the nucleon driplines, have been successfully described with mean-field models based on the Gogny interaction, the Skyrme energy functional, and the relativistic meson-exchange effective Lagrangian [1,2]. The self-consistent mean-field approach to nuclear structure represents an approximate implementation of Kohn-Sham density functional theory, which enables a description of the nuclear many-body problem in terms of a universal energy density functional. This framework, extended to take into account the most important correlations, provides a detailed microscopic description of structure phenomena associated with shell evolution in exotic nuclei. When compared to the interacting shell model, important advantages of the mean-field approach include the use of global effective nuclear interactions, the treatment of arbitrarily heavy systems including superheavy nuclei, and the intuitive picture of intrinsic shapes.

A quantitative description of shell evolution, and in particular the treatment of shape coexistence phenomena, necessitates the inclusion of many-body correlations beyond the mean-field approximation. The starting point is usually a constrained Hartree-Fock plus BCS (HF + BCS) or Hartree-Fock-Bogoliubov (HFB) calculation of the potential energy surface with the mass quadrupole components as constrained quantities. In most studies calculations have been restricted to axially symmetric, parity-conserving configurations. The erosion of spherical shell closures in nuclei far from stability leads to deformed intrinsic states and, in some cases, mean-field potential energy surfaces with almost degenerate prolate and oblate minima. To describe nuclei with soft potential energy surfaces and/or small energy differences between coexisting minima, it is necessary to explicitly consider correlation effects beyond the mean-field level. The rotational energy correction (i.e., the energy gained by the restoration of rotational symmetry) is proportional to the quadrupole deformation of the intrinsic state and can reach several MeV for a well-deformed configuration. Fluctuations of quadrupole

deformation also contribute to the correlation energy. Both types of correlations can be included simultaneously by mixing angular-momentum-projected states corresponding to different quadrupole moments. The most effective approach for configuration mixing calculations is the generator coordinate method (GCM), with multipole moments used as coordinates that generate the intrinsic wave functions.

In a series of recent papers [3–6], the angular-momentum-projected GCM with the axial quadrupole moment as the generating coordinate, and intrinsic configurations calculated in the HFB model with the finite-range Gogny interaction, has been applied in studies of shape-coexistence phenomena that result from the erosion of the $N = 20$ and $N = 28$ spherical shells in neutron-rich nuclei. Good agreement with experimental data has been obtained for the 2^+ excitation energies and $B(E2)$ transition probabilities of the $N = 28$ neutron-rich isotones [3]. The systematic study of the ground and low-lying excited states of the even-even $^{20-40}$Mg [4] is particularly interesting, because this chain of isotopes includes three spherical magic numbers: $N = 8, 20, 28$. It has been shown that the $N = 8$ shell closure is preserved, whereas deformed ground states are calculated for $N = 20$ and $N = 28$. In particular, the ground state of ^{32}Mg becomes deformed as a result of a fine balance between the energy correction associated with the restoration of rotational symmetry and the correlations induced by quadrupole fluctuations. In a similar analysis of the chain of even-even isotopes $^{20-34}$Ne [5], it has been shown that the ground state of the $N = 20$ nucleus ^{30}Ne is deformed, but less than the ground state of its isotone ^{32}Mg. The model has recently been applied in an analysis of shape coexistence and quadrupole collectivity in the neutron-deficient Pb isotopes [6]. A good qualitative agreement with available data has been found, especially for rotational bands built on coexisting low-lying oblate and prolate states.

Another very sophisticated model [7], which extends the self-consistent mean-field approach by including correlations, is based on constrained HF + BCS calculations with Skyrme effective interactions in the particle-hole channel and a density-dependent contact force in the pairing channel. Particle numbers and rotational symmetry are restored by projecting self-consistent mean-field wave functions on the correct numbers of neutrons and protons, and on angular momentum. Finally, a mixing of the projected wave functions corresponding to different quadrupole moments is performed with a discretized version of the GCM. The model has been successfully tested in the study of shape coexistence in ^{16}O [8] and in the analysis of the coexistence of spherical, deformed, and superdeformed states in ^{32}S, ^{36}Ar, ^{38}Ar, and ^{40}Ca [9]. For the doubly magic nucleus ^{16}O this parameter-free approach provides a very good description of those low-spin states, which correspond to axially and reflection-symmetric shapes, and allows the interpretation of their structure in terms of self-consistent *np-nh* states. A very important recent application is the study of low-lying collective excitation spectra of the neutron-deficient lead isotopes $^{182-194}$Pb [10,11]. A configuration mixing of angular-momentum- and particle-number-projected self-consistent mean-field states, calculated with the Skyrme SLy6 effective interaction, qualitatively reproduces the coexistence of spherical, oblate, prolate, and superdeformed prolate structures in neutron-deficient Pb nuclei.

Even though the self-consistent relativistic mean-field (RMF) framework has been employed in many studies of deformed nuclei, applications of meson-exchange and point-coupling models have so far been restricted to the mean-field level. In this work we report the first study of restoration of rotational symmetry and fluctuations of the quadrupole deformation in the framework of RMF models. We perform a GCM configuration mixing of angular-momentum-projected wave functions that are calculated in a relativistic point-coupling model.

In Sec. II we present an outline of the relativistic point-coupling model that will be used to generate mean-field wave functions with axial symmetry, introduce the formalism of the GCM, and describe in detail the procedure of configuration mixing of angular-momentum-projected wave functions. In Sec. III our model for GCM configuration mixing is investigated in a study of quadrupole dynamics in the nucleus ^{194}Hg, and ^{32}Mg is used as a test case for the configuration mixing calculation of angular-momentum-projected states. Section IV summarizes the results of the present investigation and ends with an outlook for future studies.

II. CONFIGURATION MIXING OF ANGULAR-MOMENTUM-PROJECTED MEAN-FIELD WAVE FUNCTIONS

In this section we review the self-consistent relativistic point-coupling model that will be used to generate constrained mean-field states and the solution of the corresponding single-nucleon Dirac equation in an axially symmetric harmonic oscillator basis. Starting with a short outline of the GCM, we describe the technical details of the configuration mixing of angular-momentum-projected wave functions.

A. The relativistic point-coupling model

Most applications of the self-consistent RMF framework have used the finite-range meson-exchange representation, in which the nucleus is described as a system of Dirac nucleons coupled to exchange mesons and the electromagnetic field through an effective Lagrangian. A medium dependence of the effective nuclear interaction can be introduced either by including nonlinear meson self-interaction terms in the Lagrangian or by assuming an explicit density dependence for the meson-nucleon couplings [2]. An alternative representation is formulated in terms of point-coupling (PC) (contact) nucleon-nucleon interactions [12–16]. In RMF-PC models the medium dependence of the effective interaction can be taken into account by the inclusion of higher order interaction terms, for instance six-nucleon vertices $(\bar{\psi}\psi)^3$ and eight-nucleon vertices $(\bar{\psi}\psi)^4$ and $[(\bar{\psi}\gamma_\mu\psi)(\bar{\psi}\gamma^\mu\psi)]^2$, or it can be encoded in the effective couplings (i.e., in the strength parameters of the interaction in the isoscalar and isovector channels). When employed in studies of ground-state properties of finite nuclei, the two representations produce results of comparable quality. The PC formulation, however, avoids some of the constraints

imposed in the meson-exchange picture such as, for instance, the use of the fictitious σ meson in the isoscalar-scalar channel. The self-consistent PC models are also closer in spirit to nuclear density functional theory, in which the exact energy functional, including higher order correlations, is approximated with powers and gradients of ground-state nucleon densities. The PC representation, with medium-dependent vertex functions, provides a natural framework in which chiral effective field theory can be employed to construct the nuclear energy density functional, thus establishing a link between the rich nuclear phenomenology and the underlying microscopic theory of low-energy QCD [17,18].

A detailed description of the PC model that we use in this work can be found, for instance, in Ref. [16], together with a thorough discussion of the choice of various parameter sets that determine the effective interactions. Here we only outline the essential features of the model and of its mean-field solution for a deformed axially symmetric nucleus.

The relativistic PC Lagrangian is built from basic densities and currents bilinear in the Dirac spinor field ψ of the nucleon:

$$\bar{\psi}\mathcal{O}_\tau\Gamma\psi, \quad \mathcal{O}_\tau \in \{1, \tau_i\}, \quad \Gamma \in \{1, \gamma_\mu, \gamma_5, \gamma_5\gamma_\mu, \sigma_{\mu\nu}\}. \tag{1}$$

Here τ_i are the isospin Pauli matrices and Γ generically denotes the Dirac matrices. The interaction terms of the Lagrangian are products of these bilinears. Although a general effective Lagrangian can be written as a power series in the currents $\bar{\psi}\mathcal{O}_\tau\Gamma\psi$ and their derivatives, it is well known from numerous applications of RMF models that properties of symmetric and asymmetric nuclear matter, as well as empirical ground-state properties of finite nuclei, constrain only the isoscalar-scalar (S), the isoscalar-vector (V), the isovector-vector (TV), and to a certain extent the isovector-scalar (TS) channels. In this work we consider a model with four-, six-, and eight-fermion point couplings (contact interactions) [16], defined by the Lagrangian density:

$$\begin{aligned}
\mathcal{L} &= \mathcal{L}^{\text{free}} + \mathcal{L}^{\text{4f}} + \mathcal{L}^{\text{hot}} + \mathcal{L}^{\text{der}} + \mathcal{L}^{\text{em}},\\
\mathcal{L}^{\text{free}} &= \bar{\psi}(\mathrm{i}\gamma_\mu\partial^\mu - m)\psi,\\
\mathcal{L}^{\text{4f}} &= -\tfrac{1}{2}\alpha_{\text{S}}(\bar{\psi}\psi)(\bar{\psi}\psi) - \tfrac{1}{2}\alpha_{\text{V}}(\bar{\psi}\gamma_\mu\psi)(\bar{\psi}\gamma^\mu\psi)\\
&\quad -\tfrac{1}{2}\alpha_{\text{TS}}(\bar{\psi}\vec{\tau}\psi)\cdot(\bar{\psi}\vec{\tau}\psi)\\
&\quad -\tfrac{1}{2}\alpha_{\text{TV}}(\bar{\psi}\vec{\tau}\gamma_\mu\psi)\cdot(\bar{\psi}\vec{\tau}\gamma^\mu\psi),\\
\mathcal{L}^{\text{hot}} &= -\tfrac{1}{3}\beta_{\text{S}}(\bar{\psi}\psi)^3 - \tfrac{1}{4}\gamma_{\text{S}}(\bar{\psi}\psi)^4\\
&\quad -\tfrac{1}{4}\gamma_{\text{V}}[(\bar{\psi}\gamma_\mu\psi)(\bar{\psi}\gamma^\mu\psi)]^2,\\
\mathcal{L}^{\text{der}} &= -\tfrac{1}{2}\delta_{\text{S}}(\partial_\nu\bar{\psi}\psi)(\partial^\nu\bar{\psi}\psi) - \tfrac{1}{2}\delta_{\text{V}}(\partial_\nu\bar{\psi}\gamma_\mu\psi)(\partial^\nu\bar{\psi}\gamma^\mu\psi)\\
&\quad -\tfrac{1}{2}\delta_{\text{TS}}(\partial_\nu\bar{\psi}\vec{\tau}\psi)\cdot(\partial^\nu\bar{\psi}\vec{\tau}\psi)\\
&\quad -\tfrac{1}{2}\delta_{\text{TV}}(\partial_\nu\bar{\psi}\vec{\tau}\gamma_\mu\psi)\cdot(\partial^\nu\bar{\psi}\vec{\tau}\gamma^\mu\psi),\\
\mathcal{L}^{\text{em}} &= -eA_\mu\bar{\psi}[(1-\tau_3)/2]\gamma^\mu\psi - \tfrac{1}{4}F_{\mu\nu}F^{\mu\nu}.
\end{aligned} \tag{2}$$

Vectors in isospin space are denoted by arrows, and bold-faced symbols will indicate vectors in ordinary three-dimensional space. In addition to the free-nucleon Lagrangian $\mathcal{L}_{\text{free}}$, the four-fermion interaction terms are contained in $\mathcal{L}_{\text{4f}}$, and higher order terms are collected in $\mathcal{L}_{\text{hot}}$. When applied to finite nuclei the model must include the coupling $\mathcal{L}_{\text{em}}$ of the protons to the electromagnetic field A^μ, and derivative terms contained in $\mathcal{L}_{\text{der}}$. In the terms that contain $\partial_\nu(\bar{\psi}\Gamma\psi)$ the derivative is understood to act on both $\bar{\psi}$ and ψ. One could, of course, construct many more higher order interaction terms, or derivative terms of higher order, but in practice only a relatively small set of free parameters can be adjusted from the data set of ground-state nuclear properties.

The single-nucleon Dirac equation is derived from the variation of the Lagrangian equation (2) with respect to $\bar{\psi}$:

$$\{\boldsymbol{\alpha}[-i\boldsymbol{\nabla} - \boldsymbol{V}(\boldsymbol{r})] + V(\boldsymbol{r}) + \beta(m + S(\boldsymbol{r}))\}\psi_i(\boldsymbol{r}) = \epsilon_i\psi_i(\boldsymbol{r}). \tag{3}$$

The scalar and vector potentials

$$S(\boldsymbol{r}) = \Sigma_S(\boldsymbol{r}) + \tau_3\Sigma_{\text{TS}}(\boldsymbol{r}), \tag{4}$$

and

$$V^\mu(\boldsymbol{r}) = \Sigma^\mu(\boldsymbol{r}) + \tau_3\Sigma^\mu_{\text{TV}}(\boldsymbol{r}), \tag{5}$$

contain the nucleon isoscalar-scalar, isovector-scalar, isoscalar-vector, and isovector-vector self-energies defined by the following relations:

$$\Sigma_S = \alpha_S\rho_S + \beta_S\rho_S^2 + \gamma_S\rho_S^3 + \delta_S\triangle\rho_S, \tag{6}$$

$$\Sigma_{\text{TS}} = \alpha_{\text{TS}}\rho_{\text{TS}} + \delta_{\text{TS}}\triangle\rho_{\text{TS}}, \tag{7}$$

$$\Sigma^\mu = \alpha_V j^\mu + \gamma_V(j_\nu j^\nu)j^\mu + \delta_V\triangle j^\mu - eA^\mu\frac{1-\tau_3}{2}, \tag{8}$$

$$\Sigma^\mu_{\text{TV}} = \alpha_{\text{TV}} j^\mu_{\text{TV}} + \delta_{\text{TV}}\triangle j^\mu_{\text{TV}}, \tag{9}$$

respectively. Because of charge conservation, only the $3-rd$ component of the isovector densities and currents contributes to the nucleon self-energies. The local densities and currents are calculated in the *no-sea* approximation:

$$\rho_S(\boldsymbol{r}) = \sum_{i=1}^{A}\bar{\psi}_i(\boldsymbol{r})\psi_i(\boldsymbol{r}), \tag{10}$$

$$\rho_{\text{TS}}(\boldsymbol{r}) = \sum_{i=1}^{A}\bar{\psi}_i(\boldsymbol{r})\tau_3\psi_i(\boldsymbol{r}), \tag{11}$$

$$j^\mu(\boldsymbol{r}) = \sum_{i=1}^{A}\bar{\psi}_i(\boldsymbol{r})\gamma^\mu\psi_i(\boldsymbol{r}), \tag{12}$$

$$j^\mu_{\text{TV}}(\boldsymbol{r}) = \sum_{i=1}^{A}\bar{\psi}_i(\boldsymbol{r})\gamma^\mu\tau_3\psi_i(\boldsymbol{r}). \tag{13}$$

For a nucleus with A nucleons, the summation runs over all occupied states in the Fermi sea; that is, only occupied single-nucleon states with positive energy explicitly contribute to the nucleon self-energies. The energy momentum tensor determines the total energy of the nuclear system:

$$\begin{aligned}
E_{\text{RMF}} &= \int d\boldsymbol{r}\,\mathcal{E}_{\text{RMF}}(\boldsymbol{r})\\
&= \sum_i\int d\boldsymbol{r}\,\bar{\psi}_i(\boldsymbol{r})(-i\boldsymbol{\gamma}\boldsymbol{\nabla} + m)\psi_i(\boldsymbol{r})
\end{aligned}$$

$$+\int d\boldsymbol{r}\left(\frac{\alpha_S}{2}\rho_S^2+\frac{\beta_S}{3}\rho_S^3+\frac{\gamma_S}{4}\rho_S^4+\frac{\delta_S}{2}\rho_S\triangle\rho_S\right.$$
$$+\frac{\alpha_V}{2}j_\mu j^\mu+\frac{\gamma_V}{4}(j_\mu j^\mu)^2+\frac{\delta_V}{2}j_\mu\triangle j^\mu$$
$$+\frac{\alpha_{\rm TV}}{2}j^\mu_{\rm TV}(j_{\rm TV})_\mu+\frac{\delta_{\rm TV}}{2}j^\mu_{\rm TV}\triangle(j_{\rm TV})_\mu$$
$$\left.+\frac{\alpha_{\rm TS}}{2}\rho^2_{\rm TS}+\frac{\delta_{\rm TS}}{2}\rho_{\rm TS}\triangle\rho_{\rm TS}+\frac{e}{2}\rho_p A^0\right), \qquad (14)$$

where ρ_p denotes the proton density, and A^0 is the Coulomb potential.

In this work we only consider even-even nuclei that can be described by axially symmetric shapes. It is therefore convenient to work in cylindrical coordinates,

$$x=r_\perp\cos\phi,\qquad y=r_\perp\sin\phi,\qquad \text{and}\qquad z. \qquad (15)$$

In addition, parity, symmetry with respect to the operator $e^{-i\pi\hat{J}_y}$, and time-reversal invariance are imposed as self-consistent symmetries. Time-reversal invariance implies that the spatial components of the currents vanish in the nuclear ground state. The resulting single-nucleon Dirac equation reads

$$\{-i\boldsymbol{\alpha}\boldsymbol{\nabla}+V(\boldsymbol{r})+\beta[m+S(\boldsymbol{r})]\}\psi_i(\boldsymbol{r})=\epsilon_i\psi_i(\boldsymbol{r}). \qquad (16)$$

The eigensolutions are characterized by the projection of the total angular momentum along the symmetry axis (Ω_i), the parity (π_i), and the z component of the isospin (t_i). The Dirac spinor has the following form:

$$\psi_i(\boldsymbol{r},t)=\begin{pmatrix}f_i(\boldsymbol{r},s,t)\\ ig_i(\boldsymbol{r},s,t)\end{pmatrix}$$
$$=\frac{1}{\sqrt{2\pi}}\begin{pmatrix}f_i^+(z,r_\perp)e^{i(\Omega_i-1/2)\phi}\\ f_i^-(z,r_\perp)e^{i(\Omega_i+1/2)\phi}\\ ig_i^+(z,r_\perp)e^{i(\Omega_i-1/2)\phi}\\ ig_i^-(z,r_\perp)e^{i(\Omega_i+1/2)\phi}\end{pmatrix}\chi_{t_i}(t). \qquad (17)$$

For each solution with positive Ω,

$$\psi_i\equiv\{f_i^+,f_i^-,g_i^+,g_i^-;\Omega_i\}, \qquad (18)$$

the corresponding degenerate time-reversed state

$$\psi_{\bar{i}}=T\psi_i=\{-f_i^-,f_i^+,g_i^-,-g_i^+;-\Omega_i\} \qquad (19)$$

is obtained by acting with the time-reversal operator $T=i\sigma_yK$. For even-even nuclei, the time-reversed states i and $\bar{i}$ have identical occupation probabilities.

The single-nucleon Dirac eigenvalue equation is solved by expanding the spinors f_i and g_i [Eq. (17)] in terms of eigenfunctions of an axially symmetric harmonic oscillator potential [19]:

$$V_{\rm osc}(z,r_\perp)=\tfrac{1}{2}M\omega_z^2z^2+\tfrac{1}{2}M\omega_\perp^2r_\perp^2. \qquad (20)$$

Imposing volume conservation, the two oscillator frequencies $\hbar\omega_z$ and $\hbar\omega_\perp$ can be expressed in terms of the deformation parameter β_0 and the oscillator frequency $\hbar\omega_0$:

$$\hbar\omega_z=\hbar\omega_0e^{-\sqrt{5/4\pi}\beta_0}\quad\text{and}\quad\hbar\omega_\perp=\hbar\omega_0e^{\frac{1}{2}\sqrt{5/4\pi}\beta_0}. \qquad (21)$$

The corresponding oscillator-length parameters are $b_z=\sqrt{\hbar/M\omega_z}$ and $b_\perp=\sqrt{\hbar/M\omega_\perp}$. Because of volume conservation, $b_\perp^2b_z=b_0^3$. The basis is now specified by the two constants $\hbar\omega_0$ and β_0, and basis states are characterized by the set of quantum numbers

$$|\alpha\rangle=|n_z,n_\perp,\Lambda,m_s\rangle, \qquad (22)$$

where n_z and $n_\perp$ denote the number of nodes in the z and $r_\perp$ directions, respectively. Λ and m_s are the components of the orbital angular momentum and the spin along the symmetry axis, respectively. The eigenvalue of j_z is the z projection of the total single-nucleon angular momentum

$$\Omega=\Lambda+m_s, \qquad (23)$$

and the parity is determined by

$$\pi=(-1)^{n_z+\Lambda}. \qquad (24)$$

The eigenfunctions of the axially symmetric harmonic oscillator potential read

$$\Phi_\alpha(\boldsymbol{r},s)=\frac{N_{n_z}}{\sqrt{b_z}}H_{n_z}(\xi)e^{-\xi^2/2}\frac{N^\Lambda_{n_\perp}}{b_\perp}\sqrt{2}\eta^{\Lambda/2}$$
$$\times L^\Lambda_{n_\perp}(\eta)e^{-\eta/2}\frac{1}{2\pi}e^{i\Lambda\phi}\chi_{m_s}(s), \qquad (25)$$

with $\xi=z/b_z$ and $\eta=r_\perp^2/b_\perp^2$. The Hermite polynomials $H_n(\xi)$ and the associated Laguerre polynomials $L_n^\Lambda(\eta)$ are defined in Ref. [20]. The normalization factors are given by

$$N_{n_z}=\frac{1}{\sqrt{\sqrt{\pi}2^{n_z}n_z!}}\quad\text{and}\quad N^\Lambda_{n_\perp}=\sqrt{\frac{n_\perp!}{(n_\perp+|\Lambda|)!}}. \qquad (26)$$

The large and small components of the single-nucleon Dirac spinor [Eq. (17)] are expanded in terms of the eigenfunctions [Eq. (25)]:

$$f_i(\boldsymbol{r},s,t)=\frac{1}{\sqrt{2\pi}}\begin{pmatrix}f_i^+(z,r_\perp)e^{i(\Omega-1/2)\phi}\\ f_i^-(z,r_\perp)e^{i(\Omega+1/2)\phi}\end{pmatrix}$$
$$=\sum_\alpha^{\alpha_{\rm max}}f_i^\alpha\Phi_\alpha(\boldsymbol{r},s)\chi_{t_i}(t), \qquad (27)$$
$$g_i(\boldsymbol{r},s,t)=\frac{1}{\sqrt{2\pi}}\begin{pmatrix}g_i^+(z,r_\perp)e^{i(\Omega-1/2)\phi}\\ g_i^-(z,r_\perp)e^{i(\Omega+1/2)\phi}\end{pmatrix}$$
$$=\sum_{\tilde\alpha}^{\tilde\alpha_{\rm max}}g_i^{\tilde\alpha}\Phi_{\tilde\alpha}(\boldsymbol{r},s)\chi_{t_i}(t). \qquad (28)$$

To avoid the onset of spurious states, the quantum numbers $\tilde\alpha_{\rm max}$ and $\alpha_{\rm max}$ are chosen in such a way that the corresponding major oscillator quantum numbers $N=n_z+2n_\perp+\Lambda$ are not larger than $N_{\rm sh}+1$ for the expansion of the small components, and not larger than $N_{\rm sh}$ for the expansion of the large components [19] in order to define $N_{\rm sh}$.

For an axially deformed nucleus the map of the energy surface as a function of the quadrupole moment is obtained by imposing a constraint on the expectation value of the mass quadrupole operator. The method of quadratic constraint uses an unrestricted variation of the function

$$\langle H\rangle+\frac{C}{2}(\langle\hat{Q}\rangle-q)^2, \qquad (29)$$

where $\langle H \rangle$ is the total energy, $\langle \hat{Q} \rangle$ denotes the expectation value of the mass quadrupole operator, q is the deformation parameter, and C is the stiffness constant [21].

In addition to the self-consistent mean-field potential, for open-shell nuclei pairing correlations have to be included into the energy functional. In this work we do not consider nuclear systems very far from the valley of β stability, and therefore a good approximation for the treatment of pairing correlations is provided by the BCS formalism. Following the prescription from Ref. [16], we use a δ force in the pairing channel, supplemented with a smooth cutoff determined by a Fermi function in the single-particle energies. The pairing contribution to the total energy is given by

$$E_{\rm pair}^{p(n)} = \int \mathcal{E}_{\rm pair}^{p(n)}(\boldsymbol{r}) d\boldsymbol{r} = \frac{V_{p(n)}}{4} \int \kappa_{p(n)}^{*}(\boldsymbol{r}) \kappa_{p(n)}(\boldsymbol{r}) d\boldsymbol{r}, \quad (30)$$

for protons and neutrons, respectively. $\kappa_{p(n)}(\boldsymbol{r})$ denotes the local part of the pairing tensor, and $V_{p(n)}$ is the pairing strength parameter. Of course, for open-shell nuclei Eqs. (10)–(13) for the local densities and currents include the occupation factors of single-nucleon states. Finally, the expression for the total energy reads

$$E_{\rm tot} = \int \left[\mathcal{E}_{\rm RMF}(\boldsymbol{r}) + \mathcal{E}_{\rm pair}^{p}(\boldsymbol{r}) + \mathcal{E}_{\rm pair}^{n}(\boldsymbol{r}) \right] d\boldsymbol{r}. \quad (31)$$

The center-of-mass correction has been included by adding the expectation value

$$E_{\rm c.m.} = -\frac{\langle \hat{\boldsymbol{P}}_{\rm c.m.}^{2} \rangle}{2mA} \quad (32)$$

to the total energy, where $\boldsymbol{P}_{\rm c.m.}$ is the total momentum of a nucleus with A nucleons.

B. The generator coordinate method

The GCM is based on the assumption that, starting from a set of mean-field states $|\phi(q)\rangle$ that depend on a collective coordinate q, one can build approximate eigenstates of the nuclear Hamiltonian,

$$|\Psi_{\alpha}\rangle = \sum_{j} f_{\alpha}(q_j) |\phi(q_j)\rangle. \quad (33)$$

A detailed review of the GCM can be found in Chapter 10 of Ref. [21]. In the present study the basis states $|\phi(q)\rangle$ are Slater determinants of single-nucleon states generated by solving the constrained RMF + BCS equations, as described in the previous section. This means that we use the mass quadrupole moment as the generating coordinate q. The axially deformed mean field breaks rotational symmetry, so that the basis states $|\phi(q)\rangle$ are not eigenstates of the total angular momentum. Of course, to be able to compare theoretical predictions with data, it is necessary to construct states with good angular momentum,

$$|\Psi_{\alpha}^{\rm JM}\rangle = \sum_{j,K} f_{\alpha}^{JK}(q_j) \hat{P}_{\rm MK}^{J} |\phi(q_j)\rangle, \quad (34)$$

where $\hat{P}_{\rm MK}^{J}$ denotes the angular-momentum-projection operator, given by

$$\hat{P}_{\rm MK}^{J} = \frac{2J+1}{8\pi^2} \int d\Omega D_{\rm MK}^{J*}(\Omega) \hat{R}(\Omega). \quad (35)$$

Integration is performed over the three Euler angles α, β, and γ. $D_{\rm MK}^{J}(\Omega) = e^{-iM\alpha} d_{\rm MK}^{J}(\beta) e^{-iK\gamma}$ is the Wigner function [22], and $\hat{R}(\Omega) = e^{-i\alpha \hat{J}_z} e^{-i\beta \hat{J}_y} e^{-i\gamma \hat{J}_z}$ is the rotation operator. The weight functions $f_{\alpha}^{JK}(q_j)$ are determined from the variation

$$\delta E^{J} = \delta \frac{\langle \Psi_{\alpha}^{\rm JM} | \hat{H} | \Psi_{\alpha}^{\rm JM} \rangle}{\langle \Psi_{\alpha}^{\rm JM} | \Psi_{\alpha}^{\rm JM} \rangle} = 0, \quad (36)$$

that is, by requiring that the expectation value of the energy is stationary with respect to an arbitrary variation δf_{α}^{JK}. This leads to the Hill-Wheeler equation,

$$\sum_{j,K} f_{\alpha}^{JK}(q_j) \big(\langle \phi(q_i) | \hat{H} \hat{P}_{\rm MK}^{J} | \phi(q_j) \rangle - E_{\alpha}^{J} \langle \phi(q_i) | \hat{P}_{\rm MK}^{J} | \phi(q_j) \rangle \big) = 0. \quad (37)$$

The restriction to axially symmetric configurations ($\hat{J}_z |\phi(q)\rangle = 0$) simplifies the problem considerably, because in this case the integrals over the Euler angles α and γ can be performed analytically. For an arbitrary multipole operator $\hat{Q}_{\lambda\mu}$ one thus finds

$$\langle \phi(q_i) | \hat{Q}_{\lambda\mu} \hat{P}_{\rm MK}^{J} | \phi(q_j) \rangle = \frac{2J+1}{2} \delta_{M-\mu} \delta_{K0} \int_{0}^{\pi} \sin\beta d_{-\mu 0}^{J*}(\beta) \times \langle \phi(q_i) | \hat{Q}_{\lambda\mu} e^{-i\beta \hat{J}_y} | \phi(q_j) \rangle d\beta. \quad (38)$$

By using the identity $e^{i\beta \hat{J}_y} = e^{-i\pi \hat{J}_z} e^{-i\beta \hat{J}_y} e^{i\pi \hat{J}_z}$, together with parity, and the symmetry with respect to the operator $e^{-i\pi \hat{J}_y}$, the integration interval in Eq. (38) can be reduced from $[0, \pi]$ to $[0, \pi/2]$:

$$\langle \phi(q_i) | \hat{Q}_{\lambda\mu} \hat{P}_{\rm MK}^{J} | \phi(q_j) \rangle = (2J+1) \frac{1+(-1)^J}{2} \delta_{M-\mu} \delta_{K0} \int_{0}^{\pi/2} \sin\beta d_{-\mu 0}^{J*}(\beta) \langle \phi(q_i) | \times \hat{Q}_{\lambda\mu} e^{-i\beta \hat{J}_y} | \phi(q_j) \rangle d\beta. \quad (39)$$

We notice that this expression vanishes for odd values of angular momentum J (i.e., the projected quantities are defined only for even values of J).

The norm overlap kernel

$$\mathcal{N}^{J}(q_i, q_j) = \langle \phi(q_i) | \hat{P}_{\rm MK}^{J} | \phi(q_j) \rangle = (2J+1) \frac{1+(-1)^J}{2} \delta_{M0} \delta_{K0} \int_{0}^{\pi/2} \sin\beta d_{00}^{J*}(\beta) \times \langle \phi(q_i) | e^{-i\beta \hat{J}_y} | \phi(q_j) \rangle d\beta, \quad (40)$$

can be evaluated by employing the generalized Wick theorem [7,23–25]:

$$n(q_i, q_j; \beta) \equiv \langle \phi(q_i) | e^{-i\beta \hat{J}_y} | \phi(q_j) \rangle = \pm \sqrt{\det \mathcal{N}_{ab}(q_i, q_j; \beta)}. \quad (41)$$

The overlap matrix is defined as

$$\mathcal{N}_{ab}(q_i, q_j; \beta) = u_a(q_i) R_{ab}(q_i, q_j; \beta) u_b(q_j) + v_a(q_i) R_{ab}(q_i, q_j; \beta) v_b(q_j), \quad (42)$$

where u and v denote the BCS occupation probabilities, and the matrix R reads

$$R_{ab}(q_i, q_j; \beta) = \int \psi_a^\dagger(\boldsymbol{r}; q_i) e^{-i\beta \hat{J}_y} \psi_b(\boldsymbol{r}; q_j) d\boldsymbol{r}. \quad (43)$$

If Eqs. (27) and (28) are inserted in Eq. (43), the evaluation of the matrix R reduces to the calculation of matrix elements of the rotation operator in the basis of the axially symmetric harmonic oscillator:

$$R_{ab}(q_i, q_j) = \sum_{\alpha,\beta} f_a^\alpha(q_i) f_b^\beta(q_j) \langle \alpha | e^{-i\beta \hat{J}_y} | \beta \rangle + \sum_{\tilde{\alpha},\tilde{\beta}} g_a^{\tilde{\alpha}}(q_i) g_b^{\tilde{\beta}}(q_j) \langle \tilde{\alpha} | e^{-i\beta \hat{J}_y} | \tilde{\beta} \rangle. \quad (44)$$

The simplest way to evaluate these matrix elements is to express the eigenfunctions of the axially symmetric harmonic oscillator in the spherically symmetric oscillator basis. The transformation from the spherical to the axially deformed basis is given by the following expression:

$$\left| \Omega_\alpha \Lambda_\alpha n_{\perp^\alpha n_z^\alpha} \right\rangle = \sum_{nlj} S^{nlj}_{\Omega_\alpha \Lambda_\alpha n_\perp^\alpha n_z^\alpha} | nlj \Omega_\alpha \rangle, \quad (45)$$

with the transformation coefficients $S^{nlj}_{\Omega_\alpha \Lambda_\alpha n_\perp^\alpha n_z^\alpha}$ given in Ref. [26]. It must be emphasized that this transformation is only possible if $\omega_z = \omega_\perp$ [i.e., $\beta_0 = 0$ in Eq. (21)] [27,28]. In addition, the same oscillator frequency $\hbar\omega_0$ has to be used for each value of the generating coordinate q to avoid completeness problems in the GCM calculations [27]. We have used $\hbar\omega_0 = 41A^{-1/3}$. Since the choice of the two basis parameters $\hbar\omega_0$ and β_0 cannot be optimized, the convergence of the results should be carefully checked as a function of the number of oscillator shells used in the expansion of the Dirac spinors. The expression for the matrix elements is simply

$$\langle \alpha | e^{-i\beta \hat{J}_y} | \beta \rangle = \sum_{nlj} S^{nlj}_{\Omega_\alpha \Lambda_\alpha n_\perp^\alpha n_z^\alpha} S^{nlj}_{\Omega_\beta \Lambda_\beta n_\perp^\beta n_z^\beta} d^j_{\Omega_\alpha \Omega_\beta}(\beta), \quad (46)$$

where $d^j_{\Omega_\alpha \Omega_\beta}(\beta)$ denotes the Wigner rotation matrix [22]. More general transformation coefficients have been derived in Ref. [29] for the case $\omega_\perp \neq \omega_z$, but they are rather complicated and have not been used in the present analysis.

The Hamiltonian kernel

$$\mathcal{H}^J(q_i, q_j) = \langle \phi(q_i) | \hat{H} \hat{P}^J_{\mathrm{MK}} | \phi(q_j) \rangle = (2J+1) \frac{1 + (-1)^J}{2} \delta_{M0} \delta_{K0} \int_0^{\pi/2} \sin\beta d^{J*}_{00}(\beta) \times \langle \phi(q_i) | \hat{H} e^{-i\beta \hat{J}_y} | \phi(q_j) \rangle d\beta \quad (47)$$

can be calculated from the mean-field energy functional [Eq. (14)] [7,23–25], provided the modified densities

$$\tau(\boldsymbol{r}; q_i, q_j, \beta) = \sum_{a,b} v_a(q_i) v_b(q_j) \mathcal{N}^{-1}_{ba}(q_i, q_j; \beta) \bar{\psi}_a(\boldsymbol{r}; q_i) \times (-i\boldsymbol{\gamma}\boldsymbol{\nabla} + m) e^{-i\beta \hat{J}_y} \psi_b(\boldsymbol{r}; q_j), \quad (48)$$

$$\rho_S(\boldsymbol{r}; q_i, q_j, \beta) = \sum_{a,b} v_a(q_i) v_b(q_j) \mathcal{N}^{-1}_{ba}(q_i, q_j; \beta) \times \bar{\psi}_a(\boldsymbol{r}; q_i) e^{-i\beta \hat{J}_y} \psi_b(\boldsymbol{r}; q_j), \quad (49)$$

$$\rho_{\mathrm{TS}}(\boldsymbol{r}; q_i, q_j, \beta) = \sum_{a,b} v_a(q_i) v_b(q_j) \mathcal{N}^{-1}_{ba}(q_i, q_j; \beta) \times \bar{\psi}_a(\boldsymbol{r}; q_i) \tau_3 e^{-i\beta \hat{J}_y} \psi_b(\boldsymbol{r}; q_j), \quad (50)$$

$$j^\mu(\boldsymbol{r}; q_i, q_j, \beta) = \sum_{a,b} v_a(q_i) v_b(q_j) \mathcal{N}^{-1}_{ba}(q_i, q_j; \beta) \times \bar{\psi}_a(\boldsymbol{r}; q_i) \gamma^\mu e^{-i\beta \hat{J}_y} \psi_b(\boldsymbol{r}; q_j), \quad (51)$$

$$j^\mu_{\mathrm{TV}}(\boldsymbol{r}; q_i, q_j, \beta) = \sum_{a,b} v_a(q_i) v_b(q_j) \mathcal{N}^{-1}_{ba}(q_i, q_j; \beta) \times \bar{\psi}_a(\boldsymbol{r}; q_i) \gamma^\mu \tau_3 e^{-i\beta \hat{J}_y} \psi_b(\boldsymbol{r}; q_j), \quad (52)$$

are used when evaluating the expression

$$h(q_i, q_j; \beta) \equiv \langle \phi(q_i) | \hat{H} e^{-i\beta \hat{J}_y} | \phi(q_j) \rangle = \int \mathcal{E}_{\mathrm{tot}}(\boldsymbol{r}; q_i, q_j, \beta) d\boldsymbol{r}. \quad (53)$$

The computational task of evaluating the Hamiltonian and norm overlap kernels can be reduced significantly if one realizes that states with very small occupation probabilities give negligible contributions to the kernels. Such states can be excluded from the calculation, and the details of this procedure can be found in Refs. [7,25].

An additional problem arises from the fact that the basis states $|\phi(q_j)\rangle$ are not eigenstates of the proton and neutron number operators $\hat{Z}$ and $\hat{N}$. The adjustment of the Fermi energies in a BCS calculation ensures only that the average value of the nucleon number operators corresponds to the actual number of nucleons. Consequently, the wave functions $|\Psi^{\mathrm{JM}}_\alpha\rangle$ are generally not eigenstates of the nucleon number operators and, moreover, the average values of the nucleon number operators are not necessarily equal to the number of nucleons in a given nucleus. This happens because the binding energy increases with the average number of nucleons and, therefore, an unconstrained variation of the weight functions in a GCM calculation will generate a ground state with the average number of protons and neutrons larger than the actual values in a given nucleus. To restore the correct mean values of the nucleon numbers, we follow the standard prescription [25,30] and modify the Hill-Wheeler equation by replacing $h(q_i, q_j; \beta)$ with

$$h'(q_i, q_j; \beta) = h(q_i, q_j; \beta) - \lambda_p [z(q_i, q_j; \beta) - z_0] - \lambda_n [n(q_i, q_j; \beta) - n_0], \quad (54)$$

where

$$z(q_i, q_j; \beta) = \langle \phi(q_i) | \hat{Z} e^{-i\beta \hat{J}_y} | \phi(q_j) \rangle$$

and

$$n(q_i, q_j; \beta) = \langle \phi(q_i) | \hat{N} e^{-i\beta \hat{J}_y} | \phi(q_j) \rangle. \quad (55)$$

$\lambda_{p(n)}$ is the proton (neutron) Fermi energy, and z_0 and n_0 denote the desired number of protons and neutrons, respectively.

The Hill-Wheeler equation,

$$\sum_j \mathcal{H}^J(q_i, q_j) f_\alpha^J(q_j) = E_\alpha^J \sum_j \mathcal{N}^J(q_i, q_j) f_\alpha^J(q_j), \quad (56)$$

presents a generalized eigenvalue problem, and thus the weight functions $f_\alpha^J(q_i)$ are not orthogonal and cannot be interpreted as collective wave functions for the variable q. It is useful to re-express Eq. (56) in terms of another set of functions, $g_\alpha^J(q_i)$, defined by

$$g_\alpha^J(q_i) = \sum_j (\mathcal{N}^J)^{1/2}(q_i, q_j) f_\alpha^J(q_j). \quad (57)$$

With this transformation the Hill-Wheeler equation defines an ordinary eigenvalue problem

$$\sum_j \tilde{\mathcal{H}}^J(q_i, q_j) g_\alpha^J(q_j) = E_\alpha g_\alpha^J(q_i), \quad (58)$$

with

$$\tilde{\mathcal{H}}^J(q_i, q_j) = \sum_{k,l} (\mathcal{N}^J)^{-1/2}(q_i, q_k) \mathcal{H}^J(q_k, q_l) (\mathcal{N}^J)^{-1/2}(q_l, q_j). \quad (59)$$

The functions $g_\alpha^J(q_i)$ are orthonormal and play the role of collective wave functions.

In practice, the first step in the solution of Eq. (56) is the diagonalization of the norm overlap kernel $\mathcal{N}^J(q_i, q_j)$ [Eq. (40)]:

$$\sum_j \mathcal{N}^J(q_i, q_j) u_k(q_j) = n_k u_k(q_i). \quad (60)$$

Since the basis functions $|\phi(q_i)\rangle$ are not linearly independent, many of the eigenvalues n_k are very close to zero. The corresponding eigenfunctions $u_k(q_i)$ are rapidly oscillating and carry very little physical information. However, owing to numerical uncertainties, their contribution to $\tilde{\mathcal{H}}^J(q_i, q_j)$ can be large, and these states should be removed from the basis. From the remaining states one builds the collective Hamiltonian

$$\mathcal{H}_{kl}^{Jc} = \frac{1}{\sqrt{n_k}} \frac{1}{\sqrt{n_l}} \sum_{i,j} u_k(q_i) \tilde{\mathcal{H}}^J(q_i, q_j) u_l(q_j), \quad (61)$$

which is subsequently diagonalized:

$$\sum_{k,l} \mathcal{H}_{kl}^{Jc} g_l^{J\alpha} = E_\alpha^J g_k^{J\alpha}. \quad (62)$$

The solution determines both the ground-state energy and the energies of excited states, for each value of the angular momentum J. The collective wave functions $g_\alpha^J(q)$ and the weight functions $f_\alpha^J(q)$ are calculated from the norm overlap eigenfunctions

$$g_\alpha^J(q_i) = \sum_l g_l^{J\alpha} u_l(q_i) \quad (63)$$

and

$$f_\alpha^J(q_i) = \sum_l \frac{g_l^{J\alpha}}{\sqrt{n_l}} u_l(q_i). \quad (64)$$

Once the weight functions $f_\alpha^J(q)$ are known, it is straightforward to calculate all physical observables, such as transition probabilities and spectroscopic quadrupole moments [4]. The reduced transition probability for a transition between an initial state (J_i, α_i) and a final state (J_f, α_f) reads

$$B(E2; J_i\alpha_i \to J_f\alpha_f) = \frac{e^2}{2J_i + 1} \left| \sum_{q_f, q_i} f_{\alpha_f}^{J_f *}(q_f) \langle J_f q_f || \hat{Q}_2 || J_i q_i \rangle f_{\alpha_i}^{J_i}(q_i) \right|^2, \quad (65)$$

and the spectroscopic quadrupole moment for a state (J, α) is defined as

$$Q^{\rm spec}(J, \alpha) = e\sqrt{\frac{16\pi}{5}} \begin{pmatrix} J & 2 & J \\ J & 0 & -J \end{pmatrix} \times \sum_{q_i, q_j} f_\alpha^{J*}(q_i) \langle J q_i || \hat{Q}_2 || J q_j \rangle f_\alpha^J(q_j). \quad (66)$$

Since these quantities are calculated in the full configuration space, there is no need to introduce effective charges; hence e denotes the bare value of the proton charge. To evaluate transition probabilities and spectroscopic quadrupole moments, we will need the reduced matrix element of the quadrupole operator,

$$\langle J_f q_f || \hat{Q}_2 || J_i q_i \rangle = (2J_i + 1)(2J_f + 1) \sum_\mu \begin{pmatrix} J_i & 2 & J_f \\ -\mu & \mu & 0 \end{pmatrix} \times \int_0^{\pi/2} \sin\beta d_{-\mu 0}^{J_i *}(\beta) \times \langle \phi(q_f) | \hat{Q}_{2\mu} e^{-i\beta \hat{J}_y} | \phi(q_i) \rangle. \quad (67)$$

III. ILLUSTRATIVE CALCULATIONS

In this section we perform several illustrative configuration mixing calculations that will test our implementation of the GCM as well as the angular momentum projection. The intrinsic wave functions that are used in the configuration mixing calculation have been obtained as solutions of the self-consistent RMF equations, subject to constraint on the mass quadrupole moment. The interaction in the particle-hole channel is determined by the effective PC Lagrangian [Eq. (2)], and a density-independent δ force is used as the effective interaction in the particle-particle channel. Pairing correlations are treated within the BCS framework.

Among a number of self-consistent RMF-PC models that have been considered over the past 10 years, a few reliable and accurate phenomenological parametrizations have been adjusted and applied in the description of ground-state properties of finite nuclei on a quantitative level. In particular, based on an extensive multiparameter χ^2 minimization procedure, Bürvenich *et al*. have adjusted the PC-F1 set of coupling constants for an effective PC Lagrangian with higher order interaction terms [16]. whereas the Lagrangian of Eq. (2) contains 11 adjustable coupling constants, the PC-F1 effective interaction corresponds to a restricted set of 9 coupling parameters and does not include the isovector-scalar channel. In addition, the effective pairing interaction is determined by the strength parameters V_p and V_n, for protons and neutrons, respectively. The parameters in the particle-hole and

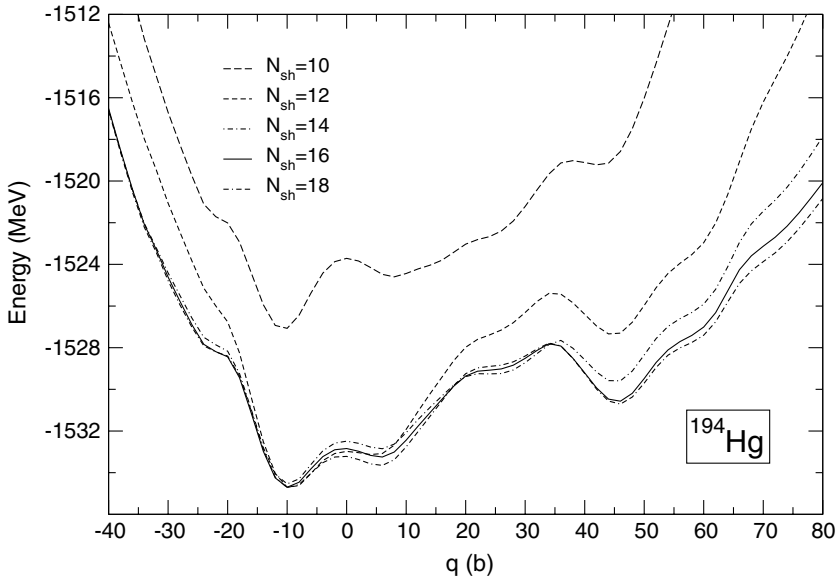

FIG. 1. The binding energy curves for ^{194}Hg, as functions of the mass quadrupole moment, calculated by expanding the Dirac spinors in 10, 12, 14, 16, and 18 oscillator shells.

particle-particle channels have been adjusted to ground-state observables (binding energies, charge radii, diffraction radii, surface thickness, and pairing gaps) of 17 spherical nuclei [16].

The PC-F1 interaction has been tested in the analysis of the equations of state of symmetric nuclear matter and neutron matter, binding energies and form factors, and shell-structure-related ground-state properties of several isotopic and isotonic chains. This interaction has also been employed in relativistic quasiparticle random phase approximation calculations of multipole giant resonances [31]. A comparison with data has shown that the RMF-PC model with the PC-F1 interaction can compete with the best phenomenological finite-range meson-exchange interactions. It should be noted, however, that PC-F1 exhibits a relatively large volume asymmetry at saturation, resulting in a very stiff equation of state for neutron matter and values that are too large for the neutron skin in finite nuclei. Modern meson-exchange effective interactions, in contrast, include an explicit medium dependence in both isoscalar and isovector channels [32–34] and thus provide an improved description of asymmetric nuclear matter and neutron matter and realistic values of the neutron skin in finite nuclei.

A. Test of the generator coordinate method: ^{194}Hg

Our first example is a test of the GCM in configuration mixing calculations for the nucleus ^{194}Hg. At this stage we do not consider angular momentum projection yet. The results of the test for the ground and excited states will be directly compared with the classical analysis of the GCM in the study of shape isomerism in ^{194}Hg by Bonche *et al.* [25]. It has to be emphasized, however, that the calculated GCM energies cannot be compared with data on a quantitative level, because, without angular momentum projection, not only is the rotational energy correction missing, but also the overlaps between states that belong to prolate and oblate minima are significantly reduced [35].

The GCM basis is constructed from self-consistent solution of the constrained single-nucleon Dirac equation on a regular mesh in the generating coordinate—the mass quadrupole moment: from $q = -40$ b to $q = 80$ b, with a spacing of $\Delta q = 2$ b. The GCM basis thus consists of 61 intrinsic states. The large and small components of Dirac spinors are expanded in terms of the axially symmetric oscillator eigenfunctions. As already pointed out in Sec. III B, the same oscillator frequency $\hbar\omega_0$ is used for each value of the generating coordinate q, and additionally the condition $\omega_z = \omega_\perp$ is imposed. Since the basis parameters are fixed to $\hbar\omega_0 = 41A^{-1/3}$ and $\beta_0 = 0$, rather then optimized, the convergence of the results with respect to the number of major oscillator shells used in the expansions Eqs. (27) and (28) has to be checked carefully.

In Fig. 1 we display the binding energy curves for ^{194}Hg, as functions of the mass quadrupole moment, calculated by expanding the Dirac spinors in 10, 12, 14, 16, and 18 oscillator shells. Obviously, at least 14 oscillator shells are necessary to obtain convergence for deformations smaller than $q = 35$ b. Larger deformations require at least 16 major oscillator shells. The absolute minimum of the binding energy curve corresponds to a slightly oblate shape ($q = -10$ b). An additional shallow minimum at excitation energy $\approx$1.5 MeV is found on the prolate side ($q = 6$ b). At much larger deformation ($q =$ 45 b) we find a third, superdeformed minimum 4.2 MeV above the first minimum of the binding energy curve. The deformations at which the three minima occur are in quantitative agreement with those calculated with the nonrelativistic constrained HF + BCS model of Ref. [25], using the SIII Skyrme effective interaction. The excitation energy of the second minimum is $\approx$1.5 MeV in both models, whereas the superdeformed minimum calculated with the SIII interaction is more than 2 MeV higher than in the present calculation. Unless stated otherwise, all calculations presented in this section have been performed in the deformed oscillator basis with $N_{\rm sh} = 16$ oscillator shells.

The first step in the solution of the modified Hill-Wheeler equation is the construction and diagonalization of the norm overlap kernel

$$\mathcal{N}(q_i, q_j) = \langle \phi(q_i) | \phi(q_j) \rangle; \tag{68}$$

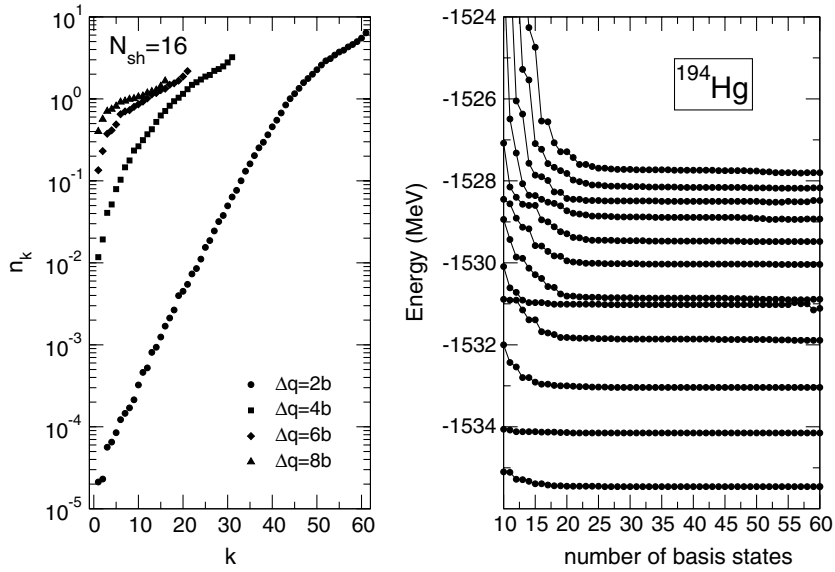

FIG. 2. The eigenvalues of the norm overlap kernel, calculated using four different values for the mesh spacing: $\Delta q = 2, 4, 6$, and 8 b (left panel). The energies of the 12 lowest GCM states plotted as functions of the dimension of the GCM basis (right panel).

see Eq. (60). Since the GCM basis states are not linearly independent, many of the norm overlap kernel eigenvalues n_k are close to zero. This is illustrated in the left panel of Fig. 2, where we display the eigenvalues n_k for four different values of the mesh spacing, ranging from $\Delta q = 2$ b to $\Delta q = 8$ b. For $\Delta q = 2$ b the overlaps between neighboring states are typically ≈ 0.8, and in the corresponding set of 61 eigenvalues we find 13 values smaller then 10^{-3}. If the mesh spacing is increased to $\Delta q = 4$ b and $\Delta q = 6$ b, the overlaps between neighboring states are reduced approximately by factors of 2 and 8, respectively. A further increase of the mesh spacing results in very small overlaps between neighboring states (≈ 0.05); that is, basis states become almost orthogonal. Except in a few test cases that will be specified explicitly, all calculations in this section have been carried out with the mesh spacing $\Delta q = 2$ b.

In the next step the GCM basis space is truncated by eliminating those eigenvectors of the norm overlap kernel, which correspond to eigenvalues smaller than a given positive constant ϵ_n. This is necessary to eliminate numerical instabilities in the diagonalization of the collective Hamiltonian [Eq. (61)]. In the right panel of Fig. 2, the energies of the 12 lowest GCM states are plotted as functions of the number of basis states. We notice that the spectrum is stable for a broad range of basis dimensions, between 25 ($\epsilon_n = 0.2$) and 55 ($\epsilon_n = 5 \times 10^{-4}$) vectors. These results can be directly compared with Fig. 4 of Ref. [25]. In the following calculations, eigenvectors of the norm overlap kernel with eigenvalues smaller than $\epsilon_n = 5 \times 10^{-4}$ are eliminated from the basis.

In Fig. 3 we plot the energies of the 15 lowest GCM states as functions of the average quadrupole moment

$$\langle q_k \rangle = \sum_j g_k^2(q_j) q_j, \tag{69}$$

calculated in oscillator bases with 10, 12, 14, and 16 oscillator shells, together with the corresponding mean-field binding energy curves. The GCM ground states are normalized to zero energy. In all four cases the average deformation of the ground state is close to the minimum of the binding energy curve, and the gain in correlation energy that results from configuration mixing is ≈ 0.8 MeV. The energies of the ground state and the two first excited states basically converge already for a basis with 12 shells. Higher excited states, however, contain sizable admixtures of basis states with larger deformations, and the corresponding energy spectrum is sensitive to the number of oscillator shells.

The GCM states can be analyzed in more detail if one plots their collective wave functions $g_k(q)$ as functions of the quadrupole moment. In Fig. 4 we display the collective wave functions for the first 14 GCM states in ^{194}Hg. The vertical dashed line denotes the position of the barrier between the main potential well and the superdeformed well. Except for the fifth state, the wave functions of the lowest nine states are concentrated in the main potential well. The fifth state obviously belongs to the superdeformed minimum; hence its energy displays a strong dependence on the number of oscillator shells (see also Fig. 3). For states with $k \geqslant 10$ the wave functions are generally spread over a wide region of deformations, both in the main and in the superdeformed well.

In Fig. 5 we plot the GCM energy spectra, calculated with 16 oscillator shells, for four values of the mesh spacing, ranging from $\Delta q = 2$ b to $\Delta q = 8$ b. The corresponding mean-field binding energy curves are also included in the figure, and their minima are placed at zero energy. Comparing with our standard value of $\Delta q = 2$ b, we notice that the low-energy part of the spectrum is accurately calculated also for $\Delta q = 4$ b. By increasing the mesh spacing to $\Delta q = 6$ b, accurate energies are obtained only for the two lowest states. With a further increase of Δq, the overlaps between neighboring states become so small that there is hardly any configuration mixing. The resulting GCM energies are very close to the energies of the basis states $|\phi(q)\rangle$.

Several additional tests, carried out in comparison with the results of Ref. [25], have shown that our implementation of the GCM is numerically stable and, therefore, it can also be used for configuration mixing calculations with angular-momentum-projected states.

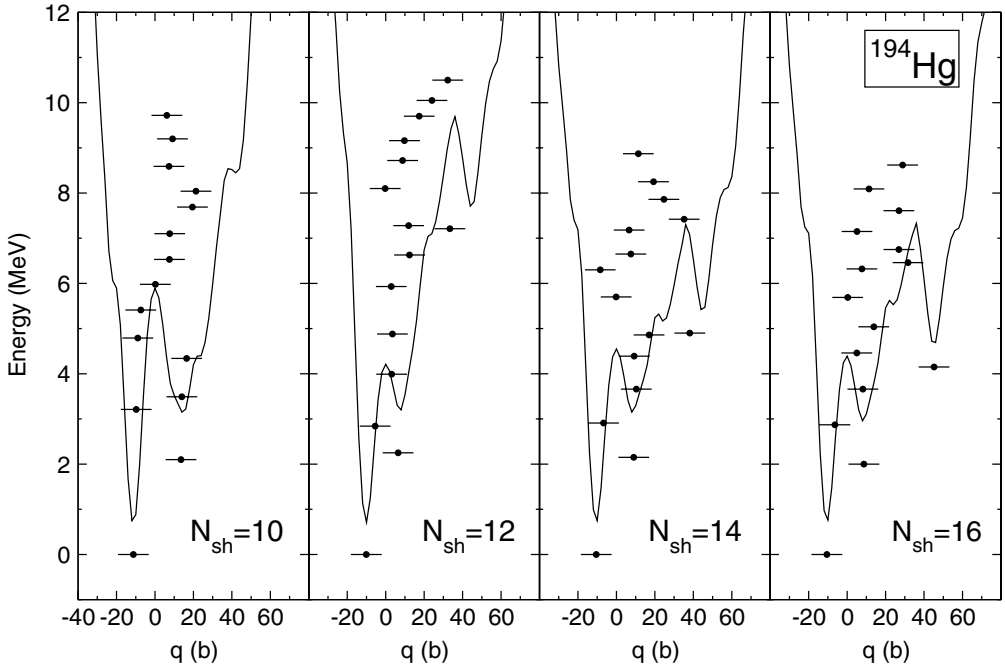

FIG. 3. The energies of the 15 lowest GCM states in ^{194}Hg, plotted as functions of the average quadrupole moment, together with the corresponding mean-field binding energy curves. The four panels correspond to calculations in oscillator bases with 10, 12, 14, and 16 major oscillator shells.

B. Test of angular momentum projection: ^{32}Mg

For a quantitative description of structure phenomena, especially in transitional deformed nuclei characterized by a coexistence of spherical and intruder configurations, calculations must explicitly include correlations related to restoration of broken symmetries. In particular, the rotational energy correction (i.e., the gain in energy obtained by projection on states with good angular momentum) can be of the order of 2–4 MeV for the ground state. Here we perform several tests of the angular momentum projection for the isotope ^{32}Mg. This nucleus belongs to the island of inversion at $N = 20$, which is characterized by the melting of the neutron shell closure and the predominance of intruder state configurations in ground states of neutron-rich systems. The structure of ^{32}Mg has been the subject of numerous experimental and theoretical studies. Several modern theoretical approaches have recently been employed in extensive studies of the erosion of the spherical $N = 20$ shell closure in this neutron-rich nucleus: the shell model [36,37], the quantum Monte Carlo shell model [38], and the angular-momentum-projected GCM based on the

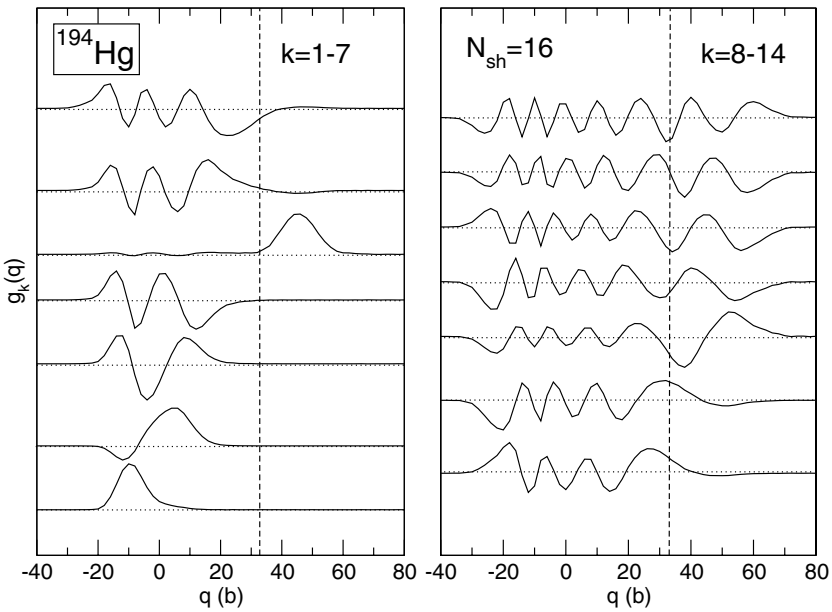

FIG. 4. GCM collective wave functions $g_k(q)$ [Eq. (57)] for the lowest 14 states in ^{194}Hg. The vertical dashed line denotes the position of the barrier separating the main and the superdeformed potential wells.

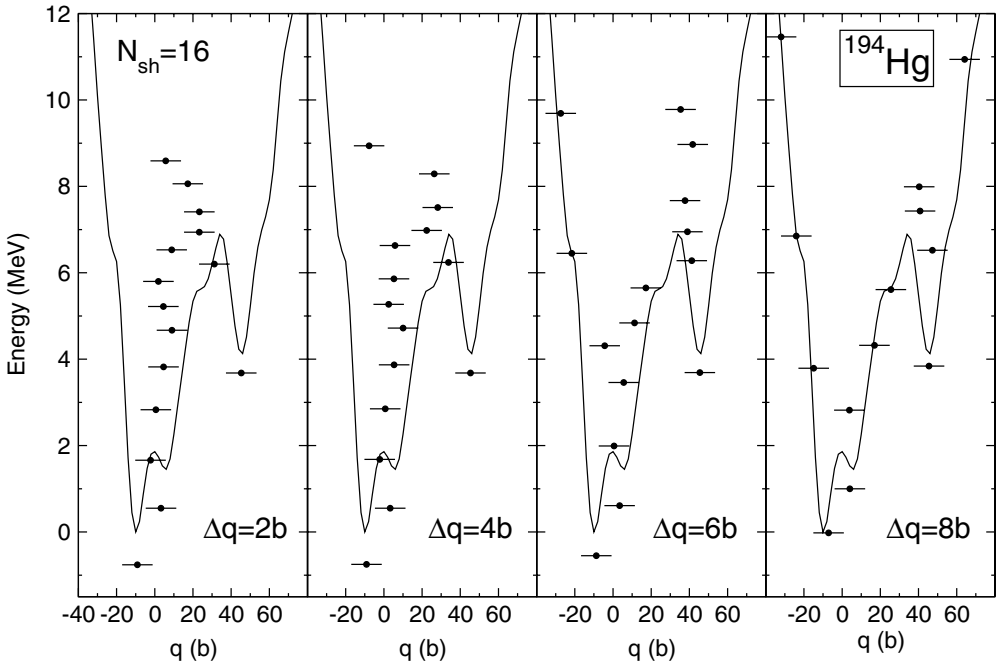

FIG. 5. The mean-field binding energy curves for ^{194}Hg, together with the energies and average quadrupole moments of the 15 lowest GCM states. Calculations have been performed using four values of the mesh spacing: $\Delta q = 2$, 4, 6, and 8 b. Zero energy is placed at the position of the minimum of the binding energy curve.

nonrelativistic Gogny interaction [4,39]. Although virtually all self-consistent mean-field models, nonrelativistic as well as relativistic, predict a spherical ground state for ^{32}Mg, the GCM calculation with the Gogny force has shown that the ground state becomes deformed as a result of the inclusion of a rotational energy correction. Both the excitation energies $E(2_1^+)$ [40] and $E(4_1^+)$ [41,42], as well as the transition probability $B(E2, 0_1^+ \rightarrow 2_1^+)$ [43,44], have been measured for ^{32}Mg. When compared to data from neighboring nuclei, the relatively low excitation energy of the first excited state, $E(2_1^+) =$ 885 keV, the large transition probability $B(E2, 0_1^+ \rightarrow 2_1^+)$, and the ratio $E(4_1^+)/E(2_1^+) = 2.6$ indicate that the ground state of ^{32}Mg is deformed.

In Fig. 6 we display the mean-field binding energy curves for ^{32}Mg as functions of the quadrupole moment, calculated with the PC-F1 relativistic PC effective interaction. The constrained mean-field equation has been solved self-consistently on a regular mesh ranging from $q = -2.2$ b to $q = 4.0$ b, with mesh spacing $\Delta q = 0.2$ b. The three curves correspond to calculations with $N_{\rm sh} = 8$, 10, and 12 major oscillator shells. For such a light system and for this range of deformations, it appears that already 10 oscillator shells are sufficient to obtain a reasonably converged mean-field binding energy curve. In the following calculations we expand the Dirac spinors in the axially deformed oscillator basis with $N_{\rm sh} = 10$ major shells. This choice is also supported by the results of Ref. [4], where correlations beyond the mean-field approximation have been studied in the framework of the angular-momentum-projected GCM with the Gogny force. In addition to a spherical ground state, the PC-F1 binding energy curves display a prolate deformed shoulder at $q = 1.5$ b, at an excitation energy of $\approx$3.5 MeV above the ground state. The binding energy curve calculated with the Gogny force is similar (see Fig. 6 of Ref. [4]), but the prolate shoulder is somewhat more pronounced and is located only $\approx$1.9 MeV above the spherical ground state. Of course, if the shoulder is too high above the spherical ground state, correlations related to the restoration of rotational symmetry and quadrupole fluctuations might not be strong enough to deform the nucleus. The different predictions for the location of the shoulder can be related to the single-particle levels calculated with the PC-F1 interaction, displayed in Fig. 7, and with the Gogny

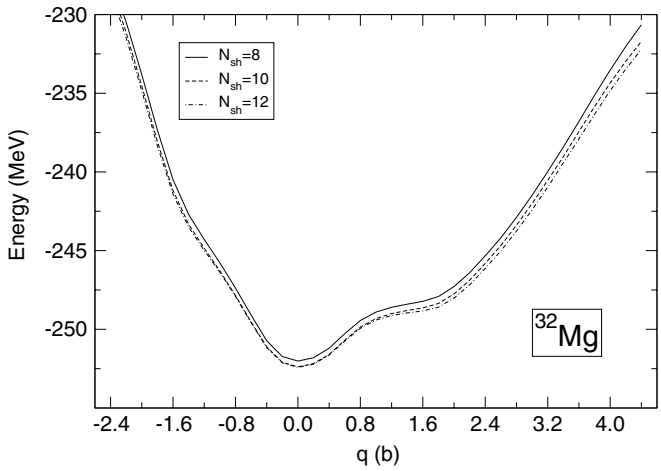

FIG. 6. The binding energy curves for ^{32}Mg, calculated from the constrained solutions of the self-consistent relativistic mean-field equations in axially deformed oscillator bases with 8, 10, and 12 major shells.

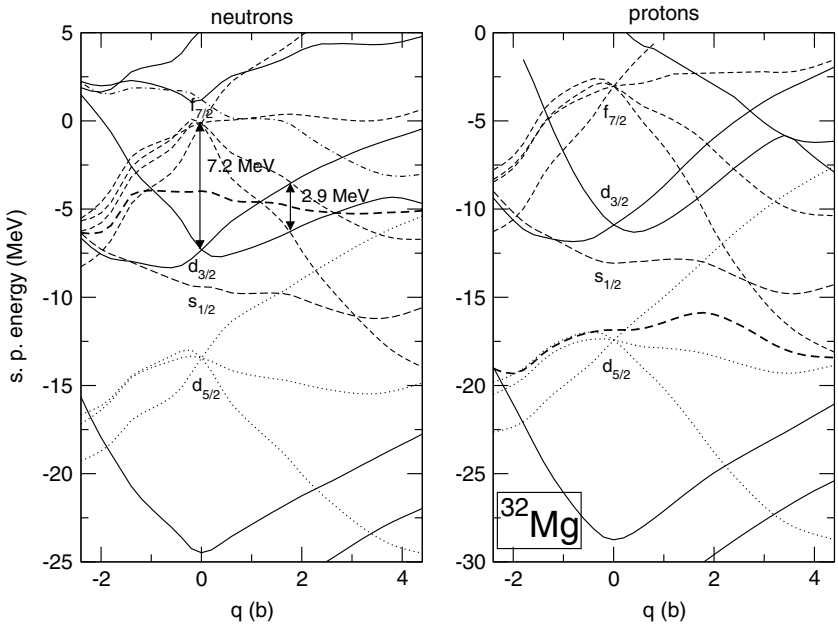

FIG. 7. The neutron (left panel) and proton (right panel) single-particle levels for ^{32}Mg, as functions of the mass quadrupole moment. The thick dashed curve denotes the position of the Fermi energy.

interaction (Fig. 5 of Ref. [4]). In these figures the eigenvalues of the corresponding mean-field Hamiltonians are plotted as functions of the quadrupole deformation. The ratio between the neutron spherical gap (7.2 MeV) and the gap at deformation $q = 1.5$ b (2.9 MeV), is $\approx$2.5 for the PC-F1 interaction, whereas the Gogny force gives a much smaller value for this ratio, $\approx$1.8. This leads to a more pronounced prolate shoulder at lower excitation energy.

The essential step in the procedure of angular momentum projection is the evaluation of the projected norm overlap kernel

$$\mathcal{N}^J(q,q) = \langle\phi(q)|P^J_{00}|\phi(q)\rangle = (2J+1)\frac{1+(-1)^J}{2} \times \int_0^{\pi/2} \sin\beta d^{J*}_{00}(\beta) n(q;\beta) d\beta, \tag{70}$$

where

$$n(q;\beta) = \langle\phi(q)|e^{-i\beta\hat{J}_y}|\phi(q)\rangle. \tag{71}$$

In several studies [35,39,45,46] it has been shown that the ansatz

$$n_{\rm app}(q;\beta) = e^{-\frac{1}{2}\langle\hat{J}^2_y\rangle\sin^2\beta}, \tag{72}$$

presents an excellent approximation for the function $n(q;\beta)$, at both small and large deformations. The expectation value $\langle\hat{J}^2_y\rangle$ as a function of the quadrupole moment is plotted in Fig. 8. This curve is in agreement with the one obtained with the Gogny interaction (see the right panel in Fig. 5 of Ref. [39]). In Fig. 9 we display the function $n(q;\beta)$ for several values of the quadrupole moment. The solid curves correspond to the approximate expression Eq. (72), whereas dots denote values obtained with the exact calculation. The comparison between the exact and approximate results provides a very useful test of the numerical procedure used in angular momentum projection. The projected norm overlap kernels, shown in Fig. 10 for the four lowest angular momenta, can be compared with those obtained using the Gogny effective interaction (see Fig. 7 of Ref. [4]). We notice that the spherical configuration is a pure 0^+ state [$\mathcal{N}^{J=0}(0,0) = 1$]. The maxima of the projected norm overlap kernels for higher angular momenta are correspondingly shifted to larger deformations.

In Fig. 11 the energies of the angular-momentum-projected states are analyzed. At this stage we do not consider configuration mixing yet, and the projected energy of the $|\phi(q)\rangle$ state reads

$$E^J(q) = \frac{\mathcal{H}^J(q,q)}{\mathcal{N}^J(q,q)}. \tag{73}$$

The angular-momentum-projected energy curves for $J^\pi = 0^+, 2^+, 4^+, 6^+$, and 8^+ are plotted, together with the corresponding mean-field binding energy curves, as functions of the quadrupole deformation. The curves obtained from solutions in axially deformed oscillator bases with $N_{\rm sh} = 8, 10$, and

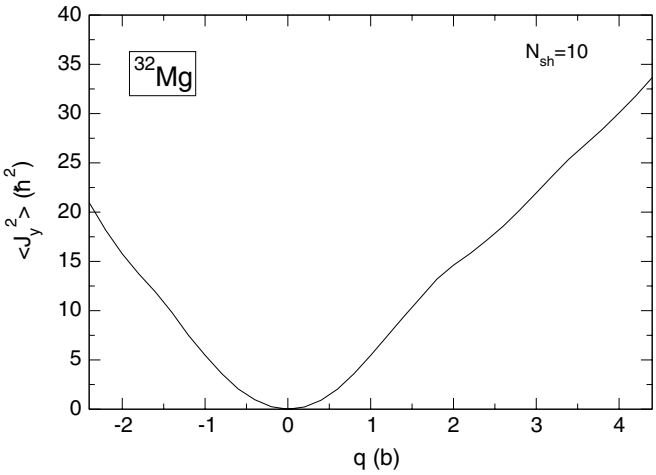

FIG. 8. The expectation value $\langle\hat{J}^2_y\rangle$ for ^{32}Mg, as a function of the mass quadrupole moment.

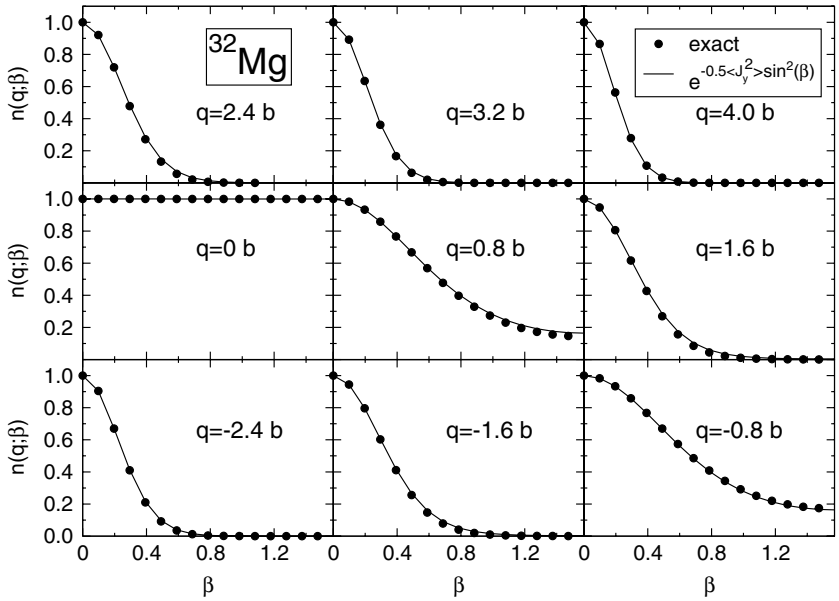

FIG. 9. A comparison between the exact values of the function $n(q;\beta)$ [Eq. (71) (dots)] and the approximate expression [Eq. (72) (curves)] for several values of the mass quadrupole moment.

12 major shells are almost identical. Since the spherical configuration is already a pure 0^+ state, there is no energy gain for $J^\pi = 0^+$ at $q = 0$. Notice that the spherical point $q = 0$ is not included in plots of $E^J(q)$ for $J \geqslant 2$. Namely, for $J \neq 0$ the quantities $\mathcal{H}^J(0,0)$ and $\mathcal{N}^J(0,0)$ are so small that their ratio [Eq. (73)] cannot be determined accurately. For higher values of the angular momentum ($J^\pi = 6^+, 8^+$ in Fig. 11) several additional configurations close to the spherical point are also characterized by very small values of the projected norm overlap kernel. These configurations can be safely omitted from the projected energy curves, because on the one hand the angular momentum projection becomes inaccurate at these points and on the other hand the corresponding angular momentum projected states would not play any role in configuration mixing calculations.

It is interesting to compare the projected energy curves with those obtained using the Gogny effective interaction (see Fig. 6 of Ref. [4]). The principal difference is seen already for the $J = 0^+$ projected energy. The PC-F1 interaction predicts two almost degenerate minima at small oblate and prolate deformations. The occurrence of degenerate oblate and prolate minima, symmetrical with respect to the spherical configuration, is a feature common to all nuclei for which the mean-field calculation predicts a spherical ground state [39]. As compared to the mean-field energy, the prolate deformed shoulder is more pronounced for the $E^{J=0}(q)$ curve, and its excitation energy has been lowered from 3.5 to 1.2 MeV by angular momentum projection. However, at the mean-field level the Gogny interaction predicts a more pronounced shoulder, only $\approx$1.9 MeV above the spherical minimum. With angular momentum projection the shoulder becomes the absolute minimum of the $J = 0$ projected energy curve; that is, when calculated with the Gogny interaction, the inclusion of the rotational energy correction leads to a deformed ground state in ^{32}Mg. In addition, the degenerate oblate and prolate minima, symmetrical with respect to $q = 0$, are predicted at slightly higher excitation energy. In the present calculation with the PC-F1 interaction, the gain in rotational energy is too small to deform the ground state of ^{32}Mg. The rotational energy correction $E_{\rm REC}$ (i.e., the difference between the mean-field and the $J^\pi = 0^+$ projected energy curves) is plotted in Fig. 12. $E_{\rm REC}$ is zero for the spherical intrinsic state, and generally it increases rather steeply for small deformations (see also Fig. 11). Our result for $E_{\rm REC}$ is very similar to the curve obtained from the Gogny mean-field potential energy (see Fig. 6 of Ref. [39]). This means that the deviation between the $J^\pi = 0^+$ projected energy curves can indeed be attributed to the difference between the PC-F1 and Gogny interactions on the mean-field level.

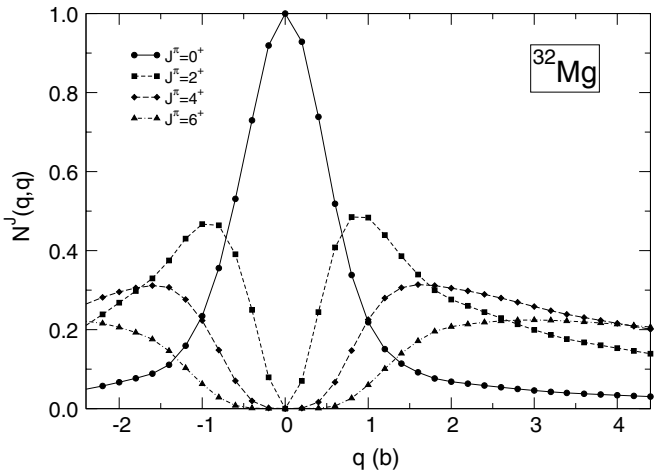

FIG. 10. Projected norm overlap kernel $\mathcal{N}^J(q,q)$ as a function of the mass quadrupole moment for ^{32}Mg.

C. Angular momentum projection and configuration mixing: ^{32}Mg

As a final test of our implementation of the GCM for RMF models, we have performed configuration mixing calculations

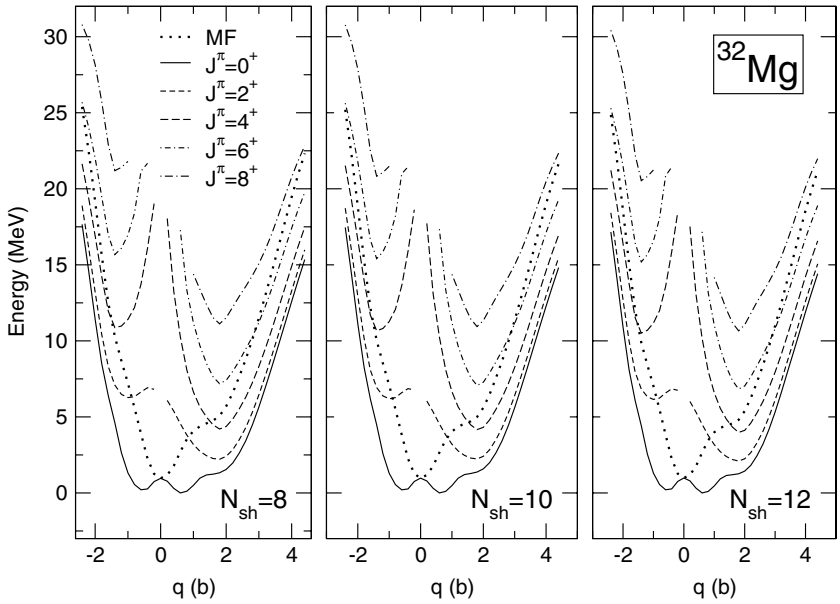

FIG. 11. Angular-momentum-projected ($J^\pi = 0^+,2^+,4^+,6^+$, and 8^+) potential energy curves for ^{32}Mg, as functions of the mass quadrupole moment. The mean-field energies are also included (thick dotted curves). The three panels correspond to solutions in axially deformed oscillator bases with 8, 10, and 12 major shells.

of the angular-momentum-projected intrinsic states for ^{32}Mg. The solution of the Hill-Wheeler matrix equation (62), with the collective Hamiltonian [Eq. (61)], determines both the ground-state energy and the energies of excited states for each value of the angular momentum J. The collective wave functions $g^J_\alpha(q)$ and the weight functions $f^J_\alpha(q)$ are calculated from the norm overlap eigenfunctions, Eqs. (63) and (64), respectively. As we have shown in Fig. 10, for $J \geqslant 2$ several points on the energy surfaces close to $q = 0$ correspond to configurations with very small values of the projected norm kernel. Since the numerical evaluation of the norm overlap and Hamiltonian kernels is not accurate in such cases, we have excluded from the configuration mixing calculation all those intrinsic configurations for which $\mathcal{N}^J(q,q) < 0.001$.

The energies and the average quadrupole moments [Eq. (69)] of the two lowest GCM states for each angular momentum are displayed in Fig. 13, together with the corresponding projected energy curves. The spectrum can be compared with the available data, and with the angular-momentum-projected GCM results obtained using the Gogny effective interaction (see Fig. 11 of Ref. [4]). Configuration mixing between the two essentially degenerate oblate and prolate minima of the $J = 0^+$ energy curve, symmetrical with respect to $q = 0$, results in the almost spherical ground state 0^+_1. When calculated with the Gogny interaction, however, the ground state is prolate deformed. The relatively large deformation is a result of a fine balance between the energy correction associated with the restoration of rotational symmetry (which favors larger deformation) and the correlations induced by quadrupole fluctuations (with mixing between oblate and prolate configurations reducing the deformation of the lowest 0^+ state).

The excitation energies of the 2^+_1, 4^+_1, and 6^+_1 GCM states are included in Table I, together with the corresponding

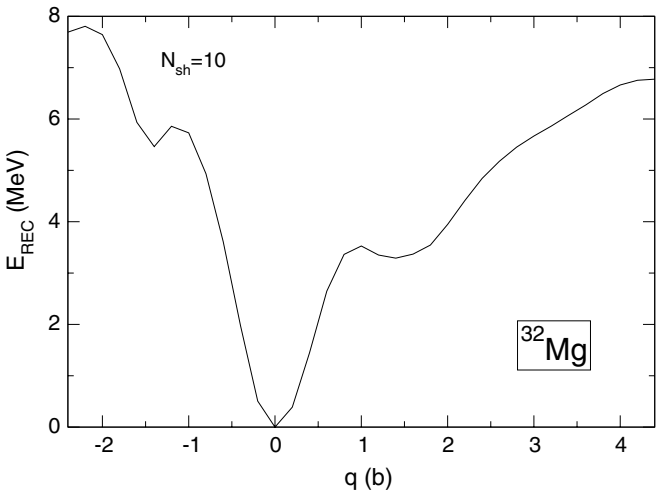

FIG. 12. Rotational energy correction as a function of the mass quadrupole moment for ^{32}Mg.

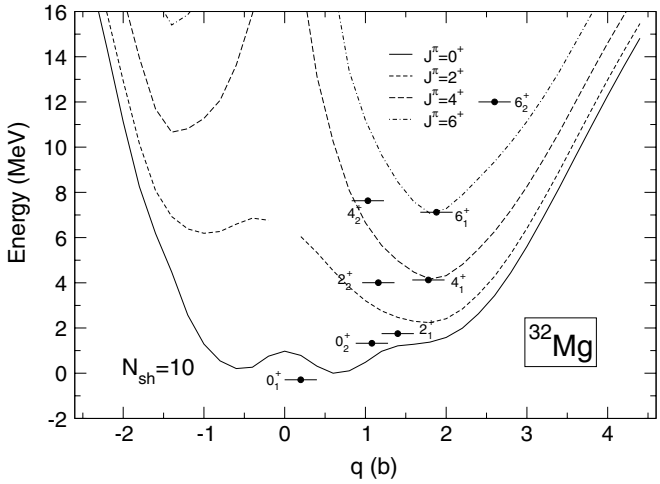

FIG. 13. The energies and the average quadrupole moments of the two lowest GCM states for each angular momentum in ^{32}Mg, together with the corresponding projected energy curves.

TABLE I. The excitation energies (in MeV) of the 2_1^+, 4_1^+, and 6_1^+ GCM states for ^{32}Mg.

	E (PC-F1)	E (Gogny)	E (exp.)
2_1^+	2.04	1.4	0.885
4_1^+	4.42	3.6	1.437
6_1^+	7.41	5.5	

energies obtained with the Gogny force and the available experimental excitation energies. Obviously, the PC-F1 interaction predicts yrast states at excitation energies that are too high, compared with the Gogny interaction or with the experimental values. In Table II we display the spectroscopic quadrupole moments of the 2_1^+, 4_1^+ and 6_1^+ GCM states for the PC-F1 and Gogny effective interactions. Although comparable in size, the quadrupole moments calculated with the PC-F1 interaction are systematically smaller. This is, of course, consistent with the lower excitation energies predicted by the Gogny force. Since the ground state is almost spherical, the calculated transition probability $B(E2; 0_1^+ \rightarrow 2_1^+) = 15.5\, e^2\,\mathrm{fm}^4$ is far too small when compared to the experimental value ($[447(57)\, e^2\,\mathrm{fm}^4]$ [44] or to the value obtained with the Gogny interaction ($395\, e^2\,\mathrm{fm}^4$) [47]. It should be noted that calculations with many nonrelativistic interactions, as for instance the Sly4 effective interaction, also exhibit similar problems [48].

The differences in the spectra predicted by the PC-F1 and Gogny interactions originate in the deviation of the corresponding mean-field binding energy curves or, more precisely, in the different neutron single-particle levels (Nilsson diagrams) calculated with the two effective interactions. Because of the large spherical gap predicted by the PC-F1 interaction, the magic number $N = 20$ persists even in such a neutron-rich system, and ^{32}Mg exhibits structure properties typical for other magic nuclei (e.g., ^{48}Ca) [3]. This is further illustrated in Fig. 14, where we display the amplitudes of the collective wave functions $|g_k^J(q)|^2$ for the two lowest GCM states of each angular momentum, together with the corresponding projected energy curves. For instance, $|g_1^0(q)|^2$ obviously reflects a configuration mixing of the prolate and oblate minima with almost equal weights, resulting in a ground state with an average quadrupole moment close to zero. The rotational energy correction for the ground state (i.e., the energy gain from angular momentum projection) is $\approx$1 MeV. Configuration mixing provides an additional gain of 0.3 MeV. Both values are in agreement with the corresponding quantities calculated for the magic ^{48}Ca nucleus [3]. The amplitudes

TABLE II. The spectroscopic quadrupole moments (in e fm^2) of the 2_1^+, 4_1^+, and 6_1^+ GCM states for ^{32}Mg.

	Q_2^{spec} (PC-F1)	Q_2^{spec} (Gogny)
2_1^+	−17.51	−19.15
4_1^+	−19.28	−26.31
6_1^+	−21.19	−30.09

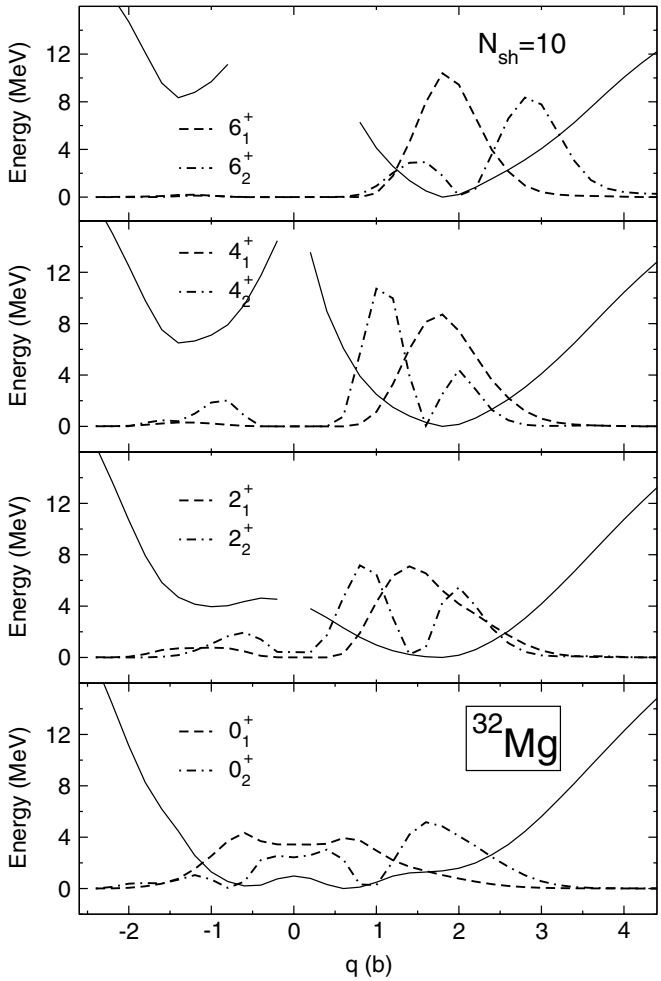

FIG. 14. Squares of the collective wave functions $|g_k^J(q)|^2$ of the two lowest GCM states for each value of the angular momentum in ^{32}Mg, together with the corresponding projected energy curves.

$|g_1^J(q)|^2$ for $J = 2, 4$, and 6 are localized in the prolate wells of the corresponding projected energy curves and, therefore, the average quadrupole moments of the states 2_1^+, 4_1^+, and 6_1^+ are close to the prolate minima. The collective wave functions $g_2^J(q)$, for $J = 2, 4$, and 6, correspond to a band based on the β vibrational state 0_2^+.

IV. SUMMARY AND OUTLOOK

The framework of self-consistent relativistic mean-field models has been very successfully employed in analyses of a variety of nuclear structure phenomena, not only in nuclei along the valley of β stability but also in exotic nuclei with extreme isospin values and close to the particle drip lines. Applications have reached a level of sophistication and accuracy comparable to the nonrelativistic Hartree-Fock (Bogoliubov) approach based on Skyrme or Gogny effective interactions. Although mean-field and pairing correlations are treated very carefully in modern RMF models, additional correlations, related to the restoration of broken symmetries and to fluctuations, have either been neglected or taken into

account in an implicit way. In this work we have introduced a model in which restoration of rotational symmetry and fluctuations of the quadrupole deformation are explicitly included in the relativistic framework.

In the specific model been developed in this work, the generator coordinate method is employed to perform configuration mixing calculations of angular-momentum-projected wave functions, calculated in a relativistic PC model. The geometry has been restricted to axially symmetric shapes, and the mass quadrupole moment is used as the generating coordinate. The intrinsic wave functions are generated from the solutions of the constrained RMF+BCS equations in an axially deformed oscillator basis.

To test our implementation of the GCM and angular momentum projection, a number of illustrative calculations have been carried out for the nuclei ^{194}Hg and ^{32}Mg. The PC-F1 parameter set [16] has been used for the effective PC Lagrangian, and the effective interaction in the particle-particle channel has been approximated by a density-independent δ force. The test of the GCM has been performed in a study of quadrupole dynamics in the nucleus ^{194}Hg, and the results have been compared with the classical analysis of the GCM in the investigation of shape isomerism in ^{194}Hg by Bonche *et al*. [25], based on the nonrelativistic constrained HF+BCS model with the SIII Skyrme effective interaction. Angular momentum projection and, finally, configuration mixing of angular-momentum-projected states, have been tested in the example of the neutron-rich nucleus ^{32}Mg, in comparison with results obtained with the angular-momentum-projected GCM based on the nonrelativistic HFB with the Gogny interaction [4,39]. The tests have been very successful, and the results obtained for the binding energy curves, projected energy curves, rotational energy corrections, ground and low-lying excited states, and collective wave functions for ^{194}Hg and ^{32}Mg are generally in very good agreement with the predictions of GCM calculations based on nonrelativistic Skyrme and Gogny interactions, respectively.

The choice of the PC-F1 relativistic effective interaction, however, does not lead to a deformed solution for the ground state of ^{32}Mg, even after the inclusion of the rotational energy correction. This result is in contrast with available data and with the configuration mixing calculation of angular-momentum-projected configurations based on the Gogny interaction. The different predictions for the ground state of ^{32}Mg can be related to the corresponding mean-field binding energy curves and, more specifically, to the different results for the size of the spherical $N = 20$ neutron gap, obtained with the Gogny and PC-F1 interactions. Even though the spherical ground state of ^{32}Mg, predicted by the PC-F1 effective interaction, is not crucial in the context of the present analysis, it points to an important problem, namely, the choice of effective interactions to be used in self-consistent calculations that go beyond the mean-field approximation and explictly include correlations, such as those considered in the present work. Virtually all global effective interactions have been adjusted to data (e.g., masses and radii) that already include correlations. However, those correlations that we wish to treat explicitly should not be included in the effective interaction in an implicit way. The solution is to adjust global effective interactions to pseudodata, obtained by subtracting correlation effects from experimental masses and radii. Approximate methods for the calculation of correlations have recently been developed [35] that will enable a systematic evaluation of correlation energies for the nuclear mass table.

Before proceeding with realistic applications of the model introduced in this work, our first task is to adjust a new global effective PC interaction that will not contain rotational energy corrections and quadrupole fluctuation correlations in an implicit way. Further developments will include the treatment of pairing fluctuations by particle number projection, the use of different generating coordinates for the neutron and proton density distributions, the description of nonaxial shapes, and the extension to odd nuclei.

ACKNOWLEDGMENTS

We thank M. Bender for useful discussions. This work has been supported in part by the Bundesministerium für Bildung und Forschung, Project No. 06 MT 193, by the Gesellschaft für Schwerionenforschung GSI, Project No. TM-RIN, by the Alexander von Humboldt Stiftung, and by the Croatian Ministry of Science, Project No. 0119250.

[1] M. Bender, P.-H. Heenen, and P.-G. Reinhard, Rev. Mod. Phys. **75**, 121 (2003).
[2] D. Vretenar, A. V. Afanasjev, G. A. Lalazissis, and P. Ring, Phys. Rep. **409**, 101 (2005).
[3] R. Rodríguez-Guzmán, J. L. Egido, and L. M. Robledo, Phys. Rev. C **65**, 024304 (2002).
[4] R. Rodríguez-Guzmán, J. L. Egido, and L. M. Robledo, Nucl. Phys. **A709**, 201 (2002).
[5] R. Rodríguez-Guzmán, J. L. Egido, and L. M. Robledo, Eur. Phys. J. A **17**, 37 (2003).
[6] R. R. Rodríguez-Guzmán, J. L. Egido, and L. M. Robledo, Phys. Rev. C **69**, 054319 (2004).
[7] A. Valor, P.-H. Heenen, and P. Bonche, Nucl. Phys. **A671**, 145 (2000).
[8] M. Bender and P.-H. Heenen, Nucl. Phys. **A713**, 390 (2003).
[9] M. Bender, H. Flocard, and P.-H. Heenen, Phys. Rev. C **68**, 044321 (2003).
[10] T. Duguet, M. Bender, P. Bonche, and P.-H. Heenen, Phys. Lett. **B559**, 201 (2003).
[11] M. Bender, P. Bonche, T. Duguet, and P.-H. Heenen, Phys. Rev. C **69**, 064303 (2004).
[12] B. A. Nikolaus, T. Hoch, and D. G. Madland, Phys. Rev. C **46**, 1757 (1992).
[13] T. Hoch, D. Madland, P. Manakos, T. Mannel, B. A. Nikolaus, and D. Strottman, Phys. Rep. **242**, 253 (1994).
[14] J. L. Friar, D. G. Madland, and B. W. Lynn, Phys. Rev. C **53**, 3085 (1996).
[15] J. J. Rusnak and R. J. Furnstahl, Nucl. Phys. **A627**, 495 (1997).
[16] T. Bürvenich, D. G. Madland, J. A. Maruhn, and P.-G. Reinhard, Phys. Rev. C **65**, 044308 (2002).

[17] P. Finelli, N. Kaiser, D. Vretenar, and W. Weise, Eur. Phys. J. A **17**, 573 (2003).
[18] P. Finelli, N. Kaiser, D. Vretenar, and W. Weise, Nucl. Phys. **A735**, 449 (2004).
[19] Y. K. Gambhir, P. Ring, and A. Thimet, Ann. Phys. (NY) **198**, 132 (1990).
[20] M. Abramowitz and I. A. Stegun, *Handbook of Mathematical Functions* (Dover, New York, 1965).
[21] P. Ring and P. Schuck, *The Nuclear Many-Body Problem* (Springer-Verlag, New York, 1980).
[22] D. A. Varshalovich, A. N. Moskalev, and V. K. Khersonskii, *Quantum Theory of Angular Momentum* (World Scientific, Singapore, 1988).
[23] R. Balian and E. Brézin, Nuovo Cimento B **64**, 37 (1969).
[24] N. Onishi and S. Yoshida, Nucl. Phys. **80**, 367 (1966).
[25] P. Bonche, J. Dobaczewski, H. Flocard, P.-H. Heenen, and J. Meyer, Nucl. Phys. **A510**, 466 (1990).
[26] J. D. Talman, Nucl. Phys. **A141**, 273 (1970).
[27] L. M. Robledo, Phys. Rev. C **50**, 2874 (1994).
[28] J. L. Egido, L. M. Robledo, and Y. Sun, Nucl. Phys. **A560**, 253 (1993).
[29] R. G. Nazmitdinov, L. M. Robledo, P. Ring, and J. L. Egido, Nucl. Phys. **A596**, 53 (1996).
[30] K. Hara, A. Hayashi, and P. Ring, Nucl. Phys. **A385**, 14 (1982).
[31] T. Nikšić, D. Vretenar, and P. Ring, Phys. Rev. C **72**, 014312 (2005).
[32] S. Typel and H. H. Wolter, Nucl. Phys. **A656**, 331 (1999).
[33] T. Nikšić, D. Vretenar, P. Finelli, and P. Ring, Phys. Rev. C **66**, 024306 (2002).
[34] G. A. Lalazissis, T. Nikšić, D. Vretenar, and P. Ring, Phys. Rev. C **71**, 024312 (2005).
[35] M. Bender, G. F. Bertsch, and P.-H. Heenen, Phys. Rev. C **69**, 034340 (2004).
[36] E. Caurier, F. Nowacki, A. Poves, and J. Retamosa, Phys. Rev. C **58**, 2033 (1998).
[37] E. Caurier, F. Nowacki, and A. Poves, Nucl. Phys. **A693**, 374 (2001).
[38] Y. Utsuno, T. Otsuka, T. Mizusaki, and M. Honma, Phys. Rev. C **60**, 054315 (1999).
[39] J. L. Egido and L. M. Robledo, in *Extended Density Functionals in Nuclear Structure Physics*, Lecture Notes in Physics, edited by G. A. Lalazissis, P. Ring, and D. Vretenar (Springer-Verlag, Heidelberg, 2004), Vol. 641.
[40] C. Détraz *et al*., Nucl. Phys. **A426**, 37 (1984).
[41] G. Klotz *et al*., Phys. Rev. C **47**, 2502 (1993).
[42] D. Guillemaud-Mueller, Eur. Phys. J. A **13**, 63 (2002).
[43] T. Motobayashi *et al*., Phys. Lett. **B346**, 9 (1995).
[44] J. A. Church *et al*., Phys. Rev. C **72**, 054320 (2005).
[45] P.-G. Reinhard and K. Goeke, Rep. Prog. Phys. **50**, 1 (1987).
[46] R. Rodríguez-Guzmán, J. L. Egido, and L. M. Robledo, Phys. Lett. **B474**, 15 (2000).
[47] R. R. Rodríguez-Guzmán, J. L. Egido, and L. M. Robledo, Phys. Rev. C **62**, 054319 (2000).
[48] P.-H. Heenen, P. Bonche, S. Ćwiok, W. Nazarewicz, and A. Valor, RIKEN Rev. **26**, 31 (2000).